Doctoral Thesis

# Spin thermoelectric energy conversion based-on hybrid magnetic insulator

Inseon Oh

Department of Materials Science and Engineering

Graduate School of UNIST

2020

# Spin thermoelectric energy conversion based-on hybrid magnetic insulator

Inseon Oh

Department of Materials Science and Engineering

Graduate School of UNIST

II

# Abstract

Thermoelectric effect (TE), which converts heat into electric voltage and vice versa, has been studied over two centuries. The interaction between heat and charge offers many applications such as thermocouples, TE power generators, and coolers. Recently, spin thermoelectric (STE) energy conversion was emerged as a next generation of thermoelectric technologies, which can convert heat into necessary electricity based-on the combination of two layers. One is a magnetic insulator, which generates pure spin currents by applied heat gradient, and the other is an adjacent non-magnetic heavy metal, which converts the generated spin currents into electricity with large spin orbit coupling. The STE device produces electricity in the orthogonal direction to the applied temperature gradient. Thus, this vertical relationship between heat flow and generated electricity allows that the generator to have the opportunity to become a large-scale device. For the improvement of the efficiency of STE energy conversion the magnetic insulator, which has small thermal conductivity and generates thermally excited magnons effectively with low wave vectors, should be developed. Then, the generated spin current should convey its spin angular momentum into adjacent conducting layer. Finally, the injected spin current should be converted into electricity via large spin orbit coupling. Thus, the potential for development of STE would be started with the development of ferromagnetic insulator which has scalable and facile processing with appropriate properties of the magnon generation layer.

In this dissertation, I present the development of ferrimagnetic insulators for the scalable STE devices by adapting various coating method and investigate the characteristics of STE as varying system temperature and applying external magnetic field. Moreover, the damping behavior in the developed hybrid magnetic insulator was investigated by analyzing ferromagnetic resonance (FMR) signals.

In chapter 3, the best representative ferrimagnetic insulator, yttrium iron garnet ($Y_3Fe_5O_{12}$, YIG), was adopted for STE with the development of facile solution-process, showing extremely low roughness, effective magnon excitation, and effective generation of spin thermoelectricity. I developed how to synthesis the nano-thickness YIG film by solution-process and how to measure and analyze the spin thermoelectric characteristics in detail. In chapter 4, I developed new type of hybrid magnetic insulator, Prussian blue analogues (PBAs), which is one of the molecule-based magnets as a thermal spin current generator. In fact, PBAs has been used as historic blue color pigments and also researched for photo-induced magnetism as a powder form. To utilize it into STE devices I fabricated it into a film form by employing electrochemical deposition (ECD) on the Cr metal, which has high spin Hall angle. Thus, the developed bilayer can be directly used as a STE generator with uniform interface. Moreover, the electrochemical deposited Cr-PBA thin film shows not only the ferrimagnetic properties, sharp crystallinity, but also the effective magnon excitation, and extremely low damping behavior which can

transport the spin current into far distance. Interestingly, the damping constant of Cr-PBA is comparable to that of YIG. We also investigated the thermal conductivity of Cr-PBA with differential 3ω method showing extremely low value, which means we can obtain relatively large temperature gradient from small amount of heat. Finally, temperature and field dependent behavior of spin thermoelectric signal reflects active generation of spin waves with low wave vectors. It means that the STE energy conversion on the Cr-PBA/Cr heterostructure occurs from great number of sub-thermal magnons. In conclusion, the observed characteristics such as effective magnon excitation, low Gilbert damping constant, and low thermal conductivity show that molecule-based magnetic films could be outstanding platforms for the generation and transmission of magnon in various spintronic applications as well as STE.

# Table of Contents

# List of figures

for the observation of reductive reaction from 0.0 V into −1.0 V. b, The generated current recorded for 10 minutes during the deposition of the Cr-PBA film at E = − 0.88 V.

Figure 21. A schematic illustration for the LSSE characterization of the Cr-PBA/Cr STE device. The temperature gradient was applied by Joule heating of a top Au line. The vertical flow of magnons pumps a pure spin current to the adjacent Cr layer. Then, the induced spin flow is converted into a longitudinal charge current producing electric field of $E_{ISHE}$.

Figure 22. Schematic illustration of top and cross-section view for the thermal conductivity measurement sample and the reference which are fabricated on the same substrate.

Figure 23. AFM images of the Cr-PBA film surface. The estimated roughness of the Cr-PBA film is 6.78 nm and 14.3 nm for 1×1 μm and 5×5 μm area, respectively.

Figure 24. The cross-sectional TEM image of a Cr-PBA/Cr bilayer deposited on an oxidized silicon substrate

Figure 25. XRD spectra of Cr-PBA films with deposition time of 600 and 1200 sec, which are 1.4 and 2.5 μm thick, respectively. Results confirm a fcc phase of PBA with main peaks 24.2 (220), 34.5 (400), 38.7 (420), and 52.8 (600)

Figure 26. The magnetic hysteresis curve of the ECD deposited Cr-PBA film measured for in-plane applied magnetic field at 100 K.

Figure 27. Temperature dependent magnetization of the ECD Cr-PBA film. The magnetization as function of temperature from 2 K to 300 K measured with in-plane magnetic field of 10 Oe. Fitting with the mean-field theory $\sim (T_c\text{-}T)^\beta$ produces $T_c \sim 223$ K.

Figure 28. Plot of the Block $T^{3/2}$ law. The temperature dependent saturation magnetization as a function of T3/2 displaying a good linearity over the wide range of temperature. Measurement was done with applying magnetic field of $H = 0.5$ T. Fitting with $M(T) = M_0(1-aT^{3/2})$ provides the value of slope $\sim 2.6\times10^{-4}$ K$^{-3/2}$, which is much higher than those of inorganic magnets.

Figure 29. Spin glass behavior of the Cr-PBA film. The temperature dependent magnetization measured for zero-field-cooled (ZFC) and field-cooled (FC) sample in applied magnetic field of 100 Oe. The strong bifurcation between ZFC and FC reflects spin glass-like behavior due to non-uniform stoichiometry of Cr-PBA film.

Figure 30. Differential 3ω measurements for the determination of the thermal conductivity of the Cr-PBA film. 2ω oscillation ($\Delta T$) as a function of logarithm frequency. Both the sample and reference display nearly the same linearity. The difference of the temperature ($\Delta T_{film}$) is calculated to be 2.47 K.

Figure 31. Estimated $\Delta T_{film}$ (black circle) and the thermal conductivity (red circle) as increasing the heater power.

Figure 32. $V_{ISHE}$ as a function of $zy$ angle of the applied magnetic field (1 T) at 100 K. Measurements were done for the Cr-PBA (1.4 μm)/Cr (10 nm) STE device. $V_{ISHE}$ upon sweeping the applied magnetic field measured with different heating currents $I_{heater} = 10$, 15, and 20 mA at 100 K.

Figure 33. $V_{ISHE}$ as a function of $zy$ angle of the applied magnetic field (1 T) at 100 K. Measurements were done for the Cr-PBA (1.4 μm)/Cr (10 nm) STE device. $V_{ISHE}$ upon sweeping the applied magnetic field measured with different heating currents $I_{heater} = 10$, 15, and 20 mA at 100 K.

Figure 34. Temperature calibration using the on-chip Au heater line. The temperature dependent

resistance of the Au heater recorded for the calibration of the temperature at the top Au layer.

Figure 35. The resistance of the Au line recorded during the stepwise increase of a Joule heating current at 100 K.

Figure 36. Schematic illustration of the temperature gradient in the STE device. The schematic figure of the temperature gradient in each layer of the STE device. The smaller the thermal conductivity is, the higher temperature gradient occurs. The studied STE device has the highest temperature gradient on the parylene layer, followed by the Cr-PBA film.

Figure 37. Heating power dependence. $\Delta V_{ISHE}$ (black circles), resistance of the Au layer ($R_{Au}$, red pentagon), and the temperature difference in Cr-PBA ($\Delta T_{Cr\text{-}PBA}$, blue stars) measured with increasing the heating current at 100 K.

Figure 38. $\Delta V_{ISHE}$ as a function of the estimated $\Delta T$ in a Cr-PBA film displaying a linear behavior. The obtained value of the slope is $\Delta V_{ISHE}/\Delta T$ is ~ 39.6 μV/K

Figure 39. Anomalous Hall effect in the Cr-PBA/Cr heterojunction. The observed VLSSE is often involved with an experimental artifact from the anomalous Hall effect (AHE) because the proximity effect could induce spontaneous magnetization in Cr layer. The AHE was measured with standard Hall geometry of the Cr-PBA/Cr bilayer at 100 K. Results clearly display absence of AHE.

Figure 40. MRs under the applied field $H_y$. The MRs of the Cr layer (a) and the top Au heater line (b) measured for the applied in-plane magnetic field ($H_y$). Results display negligible MRs in both Cr and Au electrodes. Thus, MRs of the electrodes have negligible effect in the calibration of the measured $V_{ISHE}$.

Figure 41. Temperature dependence of $V_{ISHE}$ measured with a Joule heating current, $I_{heater} = 20$ mA ($\Delta T_{Cr\text{-}PBA} = 1.17$ K). Measurements were done for the Cr-PBA (1.4 μm)/Cr (10 nm) STE device with sweeping magnetic field ($H_y$) between –5 kOe and 5 kOe. $V_{ISHE}$ ($H_y$) curves are vertically shifted for clarity.

Figure 42 Temperature dependence of $\Delta V_{ISHE} = [V_{ISHE} (+H_y) - V_{ISHE} (-H_y)]$ ($H_y = 5$ kOe), displaying a peak at around 60 K.

Figure 43. High magnetic field-dependence of $V_{ISHE}$ measured at 100 K with $I_{heater} = 10$ mA ($\Delta T_{Cr\text{-}PBA} = 0.25$ K).

Figure 44. First derivative FMR spectra of the Cr-PBA (1.4 μm)/Cr (10 nm) heterojunction at various microwave frequencies measured at 100 K. The recorded data are fitted by using the derivative of Lorentzian function.

Figure 45. Frequency dependence of resonance field $H_R$.

Figure 46. FWHM as increasing the frequency of rf field. The slope of a linear fit produces low effective Gilbert damping constant, $\alpha_{eff} \sim 7.5 \times 10^{-4}$.

Figure 47. Thickness dependent damping constants of Cr-PBA/Cr heterojunctions. For the calculation of the intrinsic damping constant of the Cr-PBA film, we measured FMR for Cr-PBA thickness ranging from 650 nm to 1.4 μm.

Figure 48. $V_{ISHE}$ ($H$) measured for Cr-PBA (1.4 μm)/Cr (10 nm) bilayer upon applying 9 GHz of microwave. The peak of $V_{ISHE}$ corresponds to the resonance field $H_R$ of FMR.

Figure 49. $V_{ISHE}$ ($H$) of Cr-PBA/Cr heterojunctions with various Cr-PBA thicknesses.

# List of tables

# List of Abbreviations

| | |
|---|---|
| **SSE** | Spin Seebeck effect |
| **ISHE** | Inverse spin Hall effect |
| **LSSE** | Longitudinal SSE |
| **SOI** | Spin-orbit interaction |
| **STE** | Spin thermoelectric |
| **FMI** | Ferrimagnetic insulator |
| **FMR** | Ferromagnetic resonance |
| **FMR-ISHE** | Ferromagnetic resonance-inverse spin Hall effect |
| **YIG** | Yttrium Iron Garnet, $Y_3Fe_5O_{12}$ |
| **CVD** | Chemical vapor deposition |
| **V[TCNE]$_{x\sim2}$** | Vanadium tetracyanoethylene |
| **PBA** | Prussian blue analogue |
| **ECD** | Electrochemical deposition |
| **LLG** | Landau-Lifshitz-Gilbert |
| **SHE** | Spin Hall effect |
| **SOC** | Spin orbit coupling |
| **2D** | Two-dimensional |
| **IREE** | Inverse Rashba Edelstein effect |
| **TI** | Topological insulator |
| **LPE** | Liquid phase epitaxy |
| **PLD** | Pulsed laser deposition |
| **GGG** | Gadolinium gallium garnet, $Gd_3Ga_5O_{12}$ |
| **XRD** | X-ray diffraction |
| **AFM** | Atomic force microscopy |
| **SQUID** | Superconducting quantum interference device |
| **VSM** | Vibrating sample magnetometer |
| **RMS** | Root mean square |
| **TEM** | Transmission electron microscope |
| **PPMS** | Physical properties measurement system |

| | |
|---|---|
| **Cr-PBA** | $Cr^{II}[Cr^{III}(CN)_6]$ Prussian blue analogue |
| **ZFC** | Zero field cool |
| **FC** | Field cool |
| **AHE** | Anomalous Hall effect |
| **MR** | Magneto-resistance |
| **TMDCs** | Transition metal dichalcogenides |

# Chapter 1. Introduction

## 1.1 Thermoelectricity

The technology of energy harvesting from light, pressure, and heat is an important topic for the future of mankind. Especially, omnipresent heat energy is promising energy source. Thermoelectric (TE) is an alternative and environmentally friendly technology to convert heat energy into useful electricity with various advantages such as no moving part, no working fluids and gases, low-noise operation, and high reliability. Conversely, the heat generation or absorption from the electricity can be occur in TE module with easy switching from cooling to heating mode. TE generation has been studied based on Seebeck effect which is built a potential difference $\Delta V$ across a metal or semiconductor along a temperature gradient ($S=\Delta V/\Delta T$). When a non-equilibrium heat flows through a conductor, especially semiconductor, the charge carriers move along the heat gradient because the carriers in the hot part move faster than those in the cold part. The reversal phenomenon is Peltier effect, which absorbs or extracts the heat by flowing electrical currents.
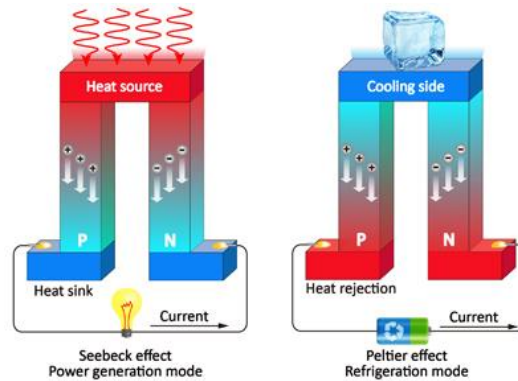


**Figure 1.** Illustration of Seebeck effect and Peltier effect.

However, the low figure of merit of TE ($ZT=S^2\sigma/\kappa$, where $S$, $\sigma$, $\kappa$, are Seebeck coefficient, electrical conductivity, and thermal conductivity, respectively) has remained as the main challenge due to several trade-off relationships between $S$ and $\sigma$ as well as the Wiedemann-Frantz law ($\kappa_e/\sigma T$ = const.). For example, materials having high electrical conductivity generally have low Seebeck coefficient. And we can't reduce electric conductivity and thermal conductivity simultaneously because the thermal conductivity relies on the transport of phonon and free electrons both. Thus, many scientists and engineers have been studied to overcome those limits with new ideas using engineering method for high

power factor and low thermal conductivity referring as "phonon glass, electron crystal" [1].

Traditionally, thermoelectric materials, such as Bi, Te, Se, and Pb, and their alloys, have been most widely used for various thermoelectric home appliances [2]. A number of complex structures of these materials, such as complex crystals, nano-composites, and thin film superlattices, have been developed to reduce lattice thermal conductivity. Such nano-material engineering has recently brought a significant improvement in the thermoelectric efficiency, $ZT \sim 2.4$ [3-5]. Recently, studies of thermoelectric properties of carbon-based materials such as conducting polymers and other carbon allotropies have been under intense research because organic materials could be cheap, flexible, abundant, easy to synthesis, and suitable for large area fabrication. The intrinsically lower thermal conductivity than that of inorganic thermoelectric materials is an additional merit regarding thermoelectric efficiency. As one of the most widely used conducting polymers, a poly (3,4-ethylenedioxythiophene):poly(styrenesulphonate) (PEDOT:PSS) could have enhanced thermoelectric performance with improved electrical conductivity and Seebeck coefficient by the secondary doping process [6, 7]. The highest ZT value of ~0.42 at room temperature was achieved by optimizing carrier concentration and morphology of the PEDOT:PSS [7]. Moreover, silicon-based thermoelectricity was studied by adapting nano-technology. Although the bulk silicon has a low ZT value around 0.01, nanowires of silicon about 20 nm thick shows substantial increasement of ZT upto 0.6 at room temperature [8, 9]. Since the concentration and type of carriers of silicon can be controlled by doping, we can enhance the ZT value by reducing the size of silicon smaller than phonon mean free path while keeping the electrical conductivity [9]. In short, we could enhance the thermoelectric performance by adapting new materials which has the properties like 'phonon glass and electron crystal' or by changing a structure and synthesis route of materials.

## 1.2 Spin thermoelectricity

### 1.2.1 Observation of Spin Seebeck effect

In 2008, Spin Seebeck effect (SSE) was firstly observed by E. Saito et al. in a magnetic metal, permalloy (Py), describing the spin-up and spin-down conduction electrons move into different way along the heat gradient like two-current model [10]. At first, it was explained that the different scattering rates and densities of spin-up and spin-down drives the thermally driven spin current. And the generated spin currents are detected by attaching Pt wire which has large spin Hall angle and clearly shows the inverse spin Hall effect (ISHE) voltage signals by sweeping magnetic field. The reason why this phenomenon drew attention is due to the long-length scale of pure spin current with several millimeter scale which is much more than several nanometer scale of typical spin diffusion lengths. Thus, the origin of SSE has become controversial issue after the discovery. In 2010, the spin Seebeck effect was also observed in a ferromagnetic semiconductor and a magnetic insulator. After that, it is suggested that the SSE originally occurs from exited spin waves (magnon). Moreover, since magnons cannot flow into opposite spin directions, the detected opposite signs of SSE at hot and cold part are proportional to the temperature difference, $T_F$-$T_N$, where $T_F$ and $T_N$ are the temperature of magnetic insulator and non-magnetic metal, respectively. Further details are described in the Chapter 2.
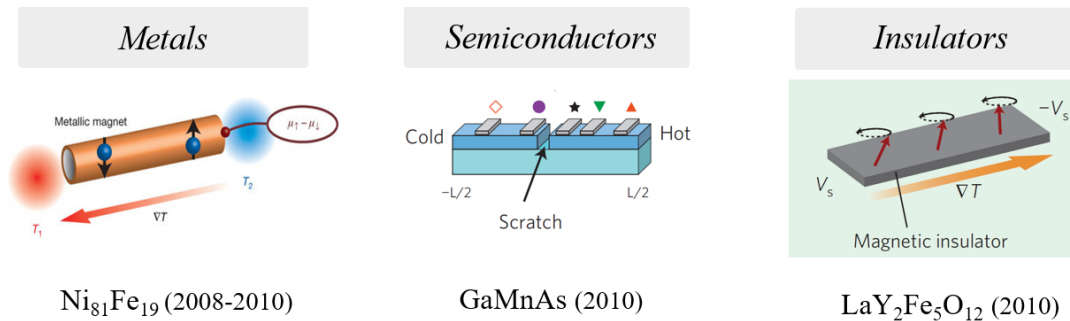


**Figure 2.** Observation of spin Seebeck effect in various ferromagnetic materials.

### 1.2.2 Geometry of Spin thermoelectricity

Transverse SSE          Longitudinal SSE
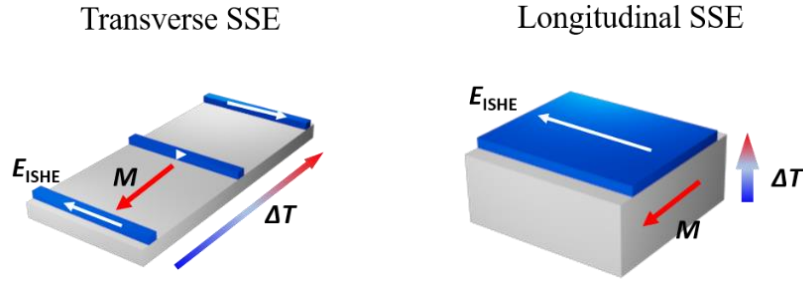


**Figure 3.** Geometry of transverse SSE and Longitudinal SSE.

There are two geometry for the detection of thermal spin current. In transverse geometry, the left side of the magnet is heated, while the right side of the magnet is cooled. Along the temperature gradient, the observed sign of SSE voltage in cold side is exactly opposite to that in the hot side with nearly identical magnitude of voltage. In the middle part, the SSE signal shows almost zero. At first these phenomena were descried that the magnetic insulator has incredibly long propagation length, but soon, it is explained by temperature difference between the adjacent metal and the magnetic insulator. With the transverse geometry, the magnon spin diffusion length is reported λ=9.4 μm in a 200 nm $Y_3Fe_5O_{12}$, Yttrium Iron Garnet(YIG) thin film at room temperature with non-local measurement geometry by applying and detecting harmonic signals which can take distinguished signal between magnon spin diffusion and thermal driven magnon currents[11].

To characterize the various transport properties of SSE in detail, a longitudinal geometry was introduced [12-14]. The generated spin current in the longitudinal geometry is parallel to the applied temperature gradient along the z-direction of the ferromagnet, producing longitudinal electrical power. This bilayer architecture of a STE device has advantages over traditional thermoelectric modules. In a longitudinal SSE (LSSE) when the magnetization $M$ of the ferromagnet is aligned along the $x$ direction and the spin current flows parallel to the temperature gradient, an ISHE-induced voltage is generated in the heavy-metal layer along the $y$ direction according to the relation, $E_{ISHE}= D_{ISHE}J\text{s} \times \sigma$, where $E_{ISHE}$, $J$s, and $\sigma$ denote the electric field induced by the ISHE, thermally generated spin current vector, and spin-polarization vector of electrons, respectively. $D_{ISHE}$ indicates the ISHE efficiency, which is associated with strength of a spin-orbit interaction (SOI) in a heavy metal film. Therefore, the applied vertical heat flux induces transverse electrical power in the ferromagnet/heavy-metal bilayer. Such a transverse energy conversion has advantages in architecturing thermoelectric devices over traditional thermoelectric modules. Not only it overcomes the trade-off relation between Seebeck coefficient ($S$) and electric conductivity ($\sigma$) and Wiedemann-Franz law ($LT = \frac{\kappa}{\sigma}$, $L$ is Lorentz number), but also it has geometrical advantage thanks to perpendicular relation rather than parallel between the heat flow and

the generated electricity. Thus, the LSSE device can be fabricated into large-scale and transparent thin film form.

In fact, the LSSE signal is suppressed significantly if a ferromagnetic metal is used in longitudinal geometry due to the short circuit current and anomalous Nernst effect as an artifact effect [12]. On the other hand, if a ferromagnetic insulator is used in longitudinal geometry device, we can attain much larger signals around several micro-voltages in micro-size devices. Moreover, since the magnetic insulator does not have conduction electrons, it can exclude the parasitic effect in LSSE. In this reason, the ferromagnetic insulators have been studied for the intrinsic mechanism of SSE with longitudinal geometry.

### 1.2.3 Spin thermoelectric energy conversion

Spin thermoelectrics (STE) as an emerging generation of TE technologies converts heat into necessary electricity based-on the combination of two layers [15]. One is a magnetic insulator, where the spin Seebeck effect (SSE) induces the propagation of thermally exited spin wave, magnon [16, 17]. The other layer is a non-magnetic heavy metal, such as, Pt, W, and Ta which has strong spin orbit coupling for the effective spin-charge conversion via the inverse spin Hall effect (ISHE) [18, 19]. This bilayer architecture of a STE device has advantages over traditional thermoelectric modules [20, 21]. Thanks to the perpendicular relation between the applied vertical heat flux and the generated electricity, STE energy conversion in the ferromagnet/heavy-metal bilayer is free from such fundamental limitations of thermoelectricity. And the simple structure of thin bilayer film can be easily adopted for transparent and flexible energy harvesting device. Moreover, the STE device is readily scalable by simply extending area of bilayer film, whereas scaling of the conventional TE module involves with series connections of alternating p-n pitches [21]. Yet, the scaling of the STE device still necessitates the development of facile film processing.

**Reference**

1.      G. A. Slack, i. D. M. R. E., *CRC handbook of Thermoelectrics, CRC, Boca Raton*. 1995; p 407-440.
2.      Wood, C., Materials for Thermoelectric Energy-Conversion. *Rep Prog Phys* **1988,** *51* (4), 459-539.
3.      Poudel, B.; Hao, Q.; Ma, Y.; Lan, Y. C.; Minnich, A.; Yu, B.; Yan, X. A.; Wang, D. Z.; Muto, A.; Vashaee, D.; Chen, X. Y.; Liu, J. M.; Dresselhaus, M. S.; Chen, G.; Ren, Z. F., High-thermoelectric performance of nanostructured bismuth antimony telluride bulk alloys. *Science* **2008,** *320* (5876), 634-638.
4.      Venkatasubramanian, R.; Siivola, E.; Colpitts, T.; O'Quinn, B., Thin-film thermoelectric devices with high room-temperature figures of merit. *Nature* **2001,** *413* (6856), 597-602.
5.      Hsu, K. F.; Loo, S.; Guo, F.; Chen, W.; Dyck, J. S.; Uher, C.; Hogan, T.; Polychroniadis, E. K.; Kanatzidis, M. G., Cubic AgPbmSbTe2+m: Bulk thermoelectric materials with high figure of merit. *Science* **2004,** *303* (5659), 818-821.
6.      Luo, J. J.; Billep, D.; Waechtler, T.; Otto, T.; Toader, M.; Gordan, O.; Sheremet, E.; Martin, J.; Hietschold, M.; Zahnd, D. R. T.; Gessner, T., Enhancement of the thermoelectric properties of PEDOT:PSS thin films by post-treatment. *J Mater Chem A* **2013,** *1* (26), 7576-7583.
7.      Kim, G. H.; Shao, L.; Zhang, K.; Pipe, K. P., Engineered doping of organic semiconductors for enhanced thermoelectric efficiency. *Nat Mater* **2013,** *12* (8), 719-723.
8.      Tang, J. Y.; Wang, H. T.; Lee, D. H.; Fardy, M.; Huo, Z. Y.; Russell, T. P.; Yang, P. D., Holey Silicon as an Efficient Thermoelectric Material. *Nano Lett* **2010,** *10* (10), 4279-4283.
9.      Rodgers, P., Nanomaterials - Silicon goes thermoelectric. *Nat Nanotechnol* **2008,** *3* (2), 76-76.
10.     Uchida, K.; Takahashi, S.; Harii, K.; Ieda, J.; Koshibae, W.; Ando, K.; Maekawa, S.; Saitoh, E., Observation of the spin Seebeck effect. *Nature* **2008,** *455* (7214), 778-781.
11.     Cornelissen, L. J.; Liu, J.; Duine, R. A.; Ben Youssef, J.; van Wees, B. J., Long-distance transport of magnon spin information in a magnetic insulator at room temperature. *Nat Phys* **2015,** *11* (12), 1022-+.
12.     Uchida, K.; Adachi, H.; Ota, T.; Nakayama, H.; Maekawa, S.; Saitoh, E., Observation of longitudinal spin-Seebeck effect in magnetic insulators. *Appl Phys Lett* **2010,** *97* (17), 172505.
13.     Uchida, K.-i.; Adachi, H.; Ota, T.; Nakayama, H.; Maekawa, S.; Saitoh, E., Observation of longitudinal spin-Seebeck effect in magnetic insulators. *Appl Phys Lett* **2010,** *97* (17).
14.     Sola, A.; Bougiatioti, P.; Kuepferling, M.; Meier, D.; Reiss, G.; Pasquale, M.; Kuschel, T.; Basso, V., Longitudinal spin Seebeck coefficient: heat flux vs. temperature difference method. *Sci Rep* **2017,** *7*, 46752.
15.     Uchida, K.-i.; Adachi, H.; Kikkawa, T.; Kirihara, A.; Ishida, M.; Yorozu, S.; Maekawa, S.; Saitoh, E. J. P. o. t. I., Thermoelectric generation based on spin Seebeck effects. *Proceedings of the IEEE* **2016,** *104* (10), 1946-1973.
16.     Ritzmann, U.; Hinzke, D.; Nowak, U., Propagation of thermally induced magnonic spin currents. *Phys Rev B* **2014,** *89* (2).
17.     Rezende, S. M.; Rodriguez-Suarez, R. L.; Cunha, R. O.; Rodrigues, A. R.; Machado, F. L. A.; Guerra, G. A. F.; Ortiz, J. C. L.; Azevedo, A., Magnon spin-current theory for the longitudinal spin-Seebeck effect. *Phys Rev B* **2014,** *89* (1).
18.     Valenzuela, S. O.; Tinkham, M., Direct electronic measurement of the spin Hall effect. *Nature* **2006,** *442* (7099), 176-9.
19.     Kimura, T.; Otani, Y.; Sato, T.; Takahashi, S.; Maekawa, S., Room-temperature reversible spin Hall effect. *Phys Rev Lett* **2007,** *98* (15), 156601.
20.     Kirihara, A.; Uchida, K.; Kajiwara, Y.; Ishida, M.; Nakamura, Y.; Manako, T.; Saitoh, E.; Yorozu, S., Spin-current-driven thermoelectric coating. *Nat Mater* **2012,** *11* (8), 686-9.
21.     Uchida, K.; Nonaka, T.; Yoshino, T.; Kikkawa, T.; Kikuchi, D.; Saitoh, E., Enhancement of Spin-Seebeck Voltage by Spin-Hall Thermopile. *Appl Phys Express* **2012,** *5* (9).

# Chapter 2. Theoretical description of spin thermoelectric generation

## 2.1 Magnon generation in magnetic insulators

### 2.1.1 Spin wave characteristics in ferrimagnetic insulators

In a ferromagnet, spins are well ordered into one direction at ground state, $T = 0$, but as temperature increases, the spin momentum starts to precess due to thermal energy. Then, the spins share its energy with neighbor spins as a form of waves to minimize their energy instead of remaining to high energy excited state. The collective excitation of spin wave in a ferromagnet is called magnon. In the view of quantum mechanics, a magnon can be regarded as a quantized spin wave. The spin wave for a one-dimensional chain of spins has dispersion relation of $\hbar\omega = 4JS(1 - cosqa)$, where q is wave vector and a is lattice constant. At small $q$, the magnon dispersion yields, $\hbar\omega \approx 2JSq^2a^2$, so that $\omega$ is proportional to $q^2$. The density of states of spin waves follows the relation, $g(q)dq \propto q^2dq$ in three dimensions, which leads to $g(\omega)d\omega \propto \omega^{1/2}d\omega$.
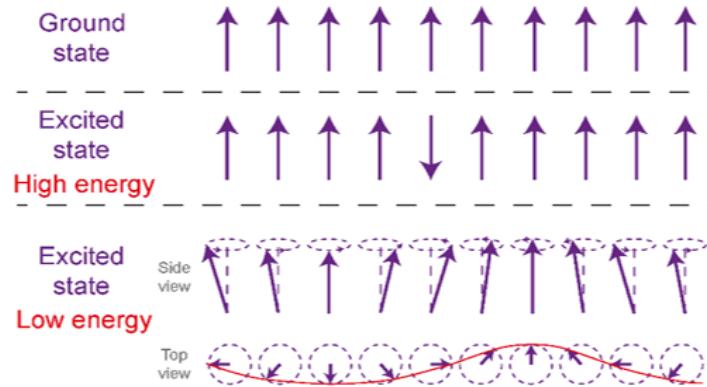


As a magnon is a quantized spin wave and obeys boson behavior, the number of magnons ($n_{\text{magnon}}$) at finite temperature, $T$, is followed by Bose-Einstein statics. Thus, the integrated magnon density of states is given by following equation,

$$n_{magnon} = \int_0^\infty \frac{g(\omega)d\omega}{exp(\hbar\omega/k_BT) - 1}.$$

If we substitute $(\hbar\omega/k_BT)$ into $x$, the equation at low temperature in three dimensions, where $g(\omega) \propto \omega^{1/2}$, yields the Bloch $T^{3/2}$ law.

$$n_{magnon} = \left(\frac{k_BT}{\hbar}\right)^{3/2} \int_0^\infty \frac{x^{1/2}dx}{e^x - 1} \propto T^{3/2}.$$

Since the thermally excited magnons reduce the total magnetization, we can observe the suppression of magnetization with increasing temperature according to the equation, which is known as the Block $T^{3/2}$ law.

$$\frac{M(0) - M(T)}{M(0)} \propto T^{3/2}$$

To investigate a magnon excitation, the temperature dependent saturation magnetization should be investigated at high magnetic field. The reduction of magnon excitations appears as the increasement of the magnetization as temperature decreases. The following equation can be used to estimate the amount of excited magnons:

$$M = M_0(1 - aT^{3/2})$$

where $M_0$ is the saturation magnetization at low temperature and $a$ is constant. From the literature, the constant $a$ is estimated to be ~ $5.2 \times 10^{-5}$ $K^{-3/2}$ [1] for YIG and ~ $7.5 \times 10^{-6}$ $K^{-3/2}$ [2] for Ni, respectively. These parameters indicate that magnon excitation in YIG is stronger than that of Ni. The transport of magnons can be exclusively studied in a ferrimagnetic insulator (FMI) because it does not have any free electrons. Thus, FMIs have been most extensively employed to generate pure spin current by SSE as well as the ferromagnetic resonance (FMR). FMI also has advantage in terms of energy conversion because it assists maintaining a vertical temperature gradient more effectively than the metallic films with low thermal conductivity. Furthermore, a magnon travels a long distance with low loss in ferrimagnetic insulator, especially in the most studied FMI YIG due to extremely low damping.

### 2.1.2 Organic- and Molecule-based magnet

Organic- and Molecule-based magnet has been studied because of their characteristic properties such as low density, transparency, magneto-optical properties, and tunable Curie temperatures. Unlike the conventional magnets, the magnetic moments of organic- and molecule-based magnets owes to electrons in $p$- and $s$- orbitals, in addition to unpaired electrons in $d$ or $f$ orbitals. The magnetic coupling in the organic- and molecule-based magnet is different from conventional magnet due to its structural characteristics. The spins of metal ions in organic based magnets interact directly with radicals of organics. On the other hand, in molecule-based magnets the molecular moiety only acts as a passage by two perpendicular empty $\pi^*$ orbitals for superexchange interaction between transition metals. By those specific routes of spin interaction, the organic- and molecule-based magnet shows the various transition temperature, the magneto-optical properties, semiconductor behaviors and spin transports [3-6].

The first study of organic based magnets, the $Fe^{III}(C_5Me_5)_2{}^+[TCNE]^-$ shows a ferromagnetic ordering at 4.8 K with high coercive field of 1 kOe [7]. The unpaired electron spins in the organic based magnet are in $p$-orbitals, unlike the ferromagnetic metal spins of $d$- or $f$- orbitals. Thus, to interact between the unpaired electrons in organic magnet, the conjugated structure is required to delocalize electrons. For a decade, the various organic- and molecule-based magnets have been designed for high Curie temperature magnet. Surprisingly, the room temperature organic based ferrimagnet, vanadium tetracyanoethylene ($V[TCNE]_{x\sim2}$), was synthesized ($T_c$=400 K, $V^{II}$ S=3/2, $[TCNE]^-$ S=1/2, thus, net magnetic moment $\sim1\mu_B$) by chemical vapor deposition (CVD) method [8, 9]. Since the $V(TCNE)_x$ is semiconductor-like with an activation energy of 0.5 eV, the spin valve effect is also reported in the Fe/Al/V[TCNE]$_x$/Al [10] and V(TCNE)$_x$/Rubrene/LAO/LSMO [3].

$$V[TCNE]_x \qquad\qquad V\text{-}Cr[Cr(CN)_6]_x$$
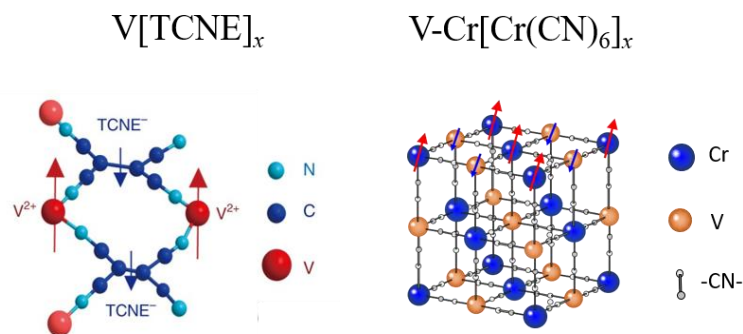


**Figure 4.** Illustration of representative examples for organic-based and molecule-based magnet

The Prussian blue analogue (PBA) is a class of the molecule based-magnets which has stable cubic structure with transition metals bridged by cyanide (-CN), $[M^1(M^2(CN)_6)_x]$. The PBA has wide range

of transition temperature according to the choice of transition metals. The combination of transition metals (V and Cr ions) showed high $T_c$ even above room temperature. Through the π-orbitals of cyanide (CN⁻), the spins in transition metals are coupled by superexchange interaction (M$^1$-CN-M$^2$) like the M-O-M superexchange occurring in oxide-based magnets [11]. Especially, V-Cr PBA shows the highest transition temperature ~373 K as powder form [12, 13]. For spintronics applications, the PBA powder has been studied for optoelectronics thanks to its magnetic bistability by an induced light [5, 14]. However, to utilize it into devices, the PBA need to be synthesized into the film form. The trial to fabricate PBA film has been studied by using electrochemical deposition (ECD) method [15-17]. Until now, the film was deposited into oxide electrode such as ITO, SnO$_2$, FTO and graphite which is chemically very stable.

Since the PBA is one of the ferrimagnetic insulators, we can utilize it into magnonics and spin thermoelectrics. The organic-based magnet, V[TCNE]$_x$, deposited on the Pt metal already shows the possibility of magnonic application with low damping constant [4]. Furthermore, the constant of temperature dependent magnetization related to Bloch's law in organic-based magnet is observed ~ $1.2 \times 10^{-4}$ K$^{-3/2}$ representing that much more magnons can be generated than ferromagnetic metals [2]. The PBA also has the possibility of spin thermoelectric applications with weak spin-lattice interaction and low thermal conductivity. Thus, the magnon excitation and propagation characteristics of PBA should be investigated by the micro-wave driven or thermally driven spin transport for its spintronic application.

## 2.2 Mechanism of spin thermoelectricity

### 2.2.1 Spin Seebeck effect

Spin Seebeck effect generates of a spin voltage by applying temperature gradient on magnetic materials [18, 19]. In case of magnetic metals, there are a number of parasitic effects caused by interaction between heat and electrons. Thus, in this section I describe only magnetic insulator which does not have any conduction electrons. And the LSSE is used to analysis the characteristic of spin Seebeck effect with limited geometry to precisely explain the mechanism of spin thermoelectricity.

<u>The propagation of thermally excited magnons in Ferrimagnetic insulators</u>

The accumulation, propagation, and spin pumping of thermally excited magnons in temperature gradients are described based on Landau-Lifshitz-Gilbert (LLG) equation, describing the precession motion of magnetization with damping.

$$\frac{d}{dt}M = -\gamma M \times H_{eff} + \frac{\alpha}{M}M \times \frac{d}{dt}M$$

In the magnet, more magnons exist in the hotter side than the colder side. This leads to a net magnon current flowing from the hotter to the colder part. This propagation of magnons can flow longer when damping constant is low. A representative material is YIG, where the magnon could propagate over 8 mm in transverse geometry [19] due to extremely low damping constant ($2 \times 10^{-4}$) [20]. For the more precise measurements of the propagation, the magnon characterization length of LSSE was estimated by controlling the thickness of YIG varying the film thickness from the 0.15 mm thin film to the 50 mm bulk [21]. The theoretical studies of the magnon propagation have shown by Jiang Xiao *et al*. [22] and Ritzmann *et al*. [23]. The propagation length of thermally excited magnons in the temperature gradients is described within an atomistic spin model with LLG equation, which is represented as the following equation [23],

$$\xi = \frac{a}{2\alpha}\sqrt{\frac{J}{2d_z}},$$

where the square-root term indicates the domain wall width, and *a*, *α* are lattice constant, and damping constant, respectively. Based on the theoretical investigation, the thickness dependent LSSE was investigated experimentally[21]. As the FMI thickness increases, the LSSE signal gradually increases and is saturated at around particular thickness. From thickness dependent LSSE measurements, we can estimate the length of thermal excited magnons with the following equation,

$$V_{\text{LSSE}} \propto 1 - \exp(-d/\xi),$$

where $d$ is the thickness of the magnet and $\xi$ is the characterization length of the LSSE. Since the $\xi$ is proportional to inverse Gilbert damping constant ($\xi \sim \alpha^{-1}$), the magnons propagate further with a lower magnetic damping.

Temperature and field dependent longitudinal spin Seebeck effect

Temperature dependent spin Seebeck effect has been studied to investigate the thermally driven-magnon behavior. As the temperature decreases, the LSSE signal increases and after peak at a certain temperature starts to decrease. This behavior was suggested by the phonon-magnon coupling because of the coincidence of the peaks between the temperature dependent-LSSE signal and -thermal conductivity [24]. However, the mismatch between the temperature dependent thermal conductivity and LSSE signal was also observed [25] which making confusions. In fact, the interaction between magnon-phonon is inevitable because they appear in the same bath. Thus, the genuine origin of temperature dependent LSSE behavior has been investigated by varying the thickness of magnetic insulator [26]. E.-J. Guo, et al investigate the temperature dependent LSSE behavior depending on not only the thickness of insulator but the interface also. As a result, as the film thickness decreases, the peak temperature of LSSE signals increases, which means the magnon propagation length of YIG is more dominant and stronger factor than phonon-magnon interaction. They measured the temperature-dependent effective magnon propagation length $\xi$, showing $\xi \sim T^{-1}$. The results coincide with $\xi \sim \alpha^{-1}$ because the damping constant of a YIG depends linearly on the temperature. The increases of $\xi$ can be limited by boundary scattering and magnon-phonon scattering. This limit is displayed as the temperature dependent LSSE signal peak because the generated magnons fully reach the metal layer. At the lower temperature, the number of thermally excited magnons decreases following the Bloch $T^{3/2}$ law.

By applying high magnetic field, we can observe the suppression of low energy magnons referred to as sub-thermal magnons. The significant reduction of LSSE signal indicates that the low-frequency magnons dominate the LSSE signal and are easily annihilated at high magnetic field. The energy of sub-thermal magnons is much smaller than magnon gap as the magnon gap opening is predicted at $\sim 12$ K in 9 T [27]. The magnetoresistance of metal layer is much smaller than the LSSE signal depression indicating negligible factor.

In conclusion, the temperature and magnetic field dependent LSSE signal shows that the dominant factor of LSSE is magnon characterization length $\xi$ which is inversely proportional to damping constant. Thus, to generate great number of magnons, we should use the magnetic insulators which

carry a low damping constant and effective excitations of sub-thermal magnons.

## 2.1.2 Spin pumping at the interface between magnet and heavy metal
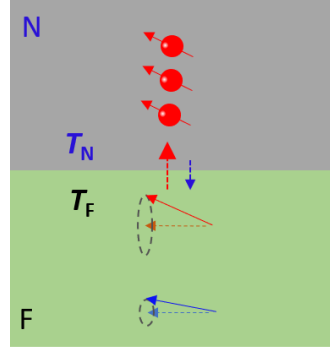


The thermally generated spin current pumps its spin angular momentum into the conduction electrons of the adjacent metal. The thermally induced spin current can exert a torque into the electrons of metal at the interface of magnet/metal junction invoking spin pumping. Then, the precession of magnetization loses torque by emitting a spin current by following equation,

$$I_s^{pump}(t) = \frac{\hbar}{4}[g_r m(t) \times \frac{dm}{dt} + g_i \frac{dm}{dt}]$$

where $g_r$, $g_i$ is the spin-mixing conductance real part and imaginary part, respectively.

However not only the pumped spin currents ($I_s^{pump}$) are generated but also the back flowed spin currents ($I_s^{back}$) occurs from the metal into the ferromagnetic insulator due to the thermal noise source.

$$I_s^{back}(t) = -\frac{M_s V}{\gamma} \gamma \frac{dm}{dt} \times h'(t)$$

Thus, the net spin current in the STE heterostructure is subtraction of the two spin currents, $I_s = I_s^{pump} - I_s^{back}$. The total spin currents is summarized into following equation,

$$I_s = \frac{\hbar \gamma}{2\pi} \frac{g_r}{M_s V_{coh}} k_B (T_F - T_N)(x),$$

where $M_s$, $\gamma$, $V_{coh}$, $k_B$ is the saturation magnetization, the gyromagnetic ratio, a magnetic coherence volume, and Boltzmann constant, respectively. The equation explains the spin Seebeck effect raises due to the temperature differences between ferromagnet and normal metal.

### 2.1.3 Spin-charge conversion

In spintronics, the generation, injection and detection of spin currents are the important phenomena to control the spintronic applications. Spin Hall effect (SHE) is a representative phenomenon for spin-charge conversion, which generates spin current from charge current due to spin orbit coupling in a conductor [28-30]. Unlike Hall effect, the SHE does not need any magnetic field because it occurs in conductors itself by spin orbit coupling (SOC). If we think about two case of SOC with relativistic effect, in case of orbiting electrons, a nucleus is circulating in the frame of an electron. Thus, a magnetic field is created in the center of the electron. The energy of SOC is represented as following equation.

$$E_{so} = -\vec{\mu} \cdot \vec{B} = \mu_B \cdot \vec{B} \approx \frac{\mu_0 \mu_B^2 Z^4}{4\pi a_0^3}$$

Thus, SOC occurs strongly in noble metals which have high atomic number such as Pt, Ta, W and so on. SOC is very weak in light atoms such as C, Si, and Cr and so on, because SOC is proportional to atomic number, $\sim Z^4$.

There are two mechanisms of SHE, intrinsic and extrinsic effect. The intrinsic mechanism occurs in the perfect crystal induced by an anomalous velocity from a Berry phase which acts as a magnetic field in momentum space. Rashba interaction is also one of the intrinsic mechanisms which occurs at the interface or surface. When the inversion symmetry of the system is broken, the large electric field can be produced, then the itinerant electrons feel effective magnetic field ($B_{eff}$). The extrinsic mechanism occurs due to non-periodic potential from the defects or imperfection of lattice which can generate potential gradient. When electrons flow in the potential gradient of the impurities, they feel the effective magnetic field ($B_{eff}$) passing by an electric field.

$$H_{so,ext} = \eta_{so}\sigma \cdot (k \times \nabla V)$$

In contrast to SHE, ISHE generates transverse charge currents from spin currents. Since ISHE has been detected even at room temperature[28, 29], it has been used extensively to detect spin current as it converts it into charge current. Thus, an ISHE electric field of a conductor is described as

$$E_{ISHE} = (\theta_{SHE}\rho_s)j_s \times \sigma,$$

where $\theta_{SHE}$ is the spin Hall angle, $\rho_s$ is the electric resistivity, $j_s$ is the spin current, and $\sigma$ is the vector of spin polarization. Platinum is most widely used paramagnetic metal with large spin Hall angle, $\sim 0.1$[31, 32]. Cr, Ni metal shows larger spin hall angle than the theoretical value in spite of the small atomic number[33, 34]. These phenomena indicate that $d$-orbital can plays a dominant role rather than atomic

number Z for SHE in 3d metals. Furthermore, Cr does not show any proximity effect on the magnetic insulator, unlike heavy metal spin detector [34]. Thus, we can use Cr metal as a pure spin current detector.

Another option for the spin-charge conversion is using inversion symmetry broken materials or interfaces. The inversion asymmetry in the bulk system invokes Dresselhaus effect and in interfaces, heterostructures, 2D systems, and semiconductor quantum wells give rise to Rashba effect. In these systems the spin currents convert into the electric currents due to the splitting of spin energy band caused by inversion asymmetry of the crystal. The degeneracy of spin in $k$-space is shown in Figure 5a. Similarly, if electric currents flow in the a 2D system with inversion asymmetry, the spin currents are generated, which is called Inverse Rashba Edelstein effect (IREE) as displayed Figure 5b. These phenomena are also called as the spin-momentum locking, *i.e.* the spin polarization is always perpendicular to the electron momentum in those system (Figure 5c). The LAO/STO interface is representative inversion asymmetry system which has large spin-charge conversion rate ($\gamma \sim 10^2\,\text{T}^{-1}\text{A}^{-1}$) [35, 36]. Topological insulator (TI) also shows the spin-momentum locking phenomena due to its energy band structure and it has been used as spin-charge conversion layer for spin thermoelectric device [37]. And 2D materials such as TMDC can be other candidates for the large spin-charge conversion rate because it is composed with heavy atoms and has inversion asymmetry. Thus, we can apply variety systems to convert spin current into electric current effectively, vice versa, in addition to noble metals.
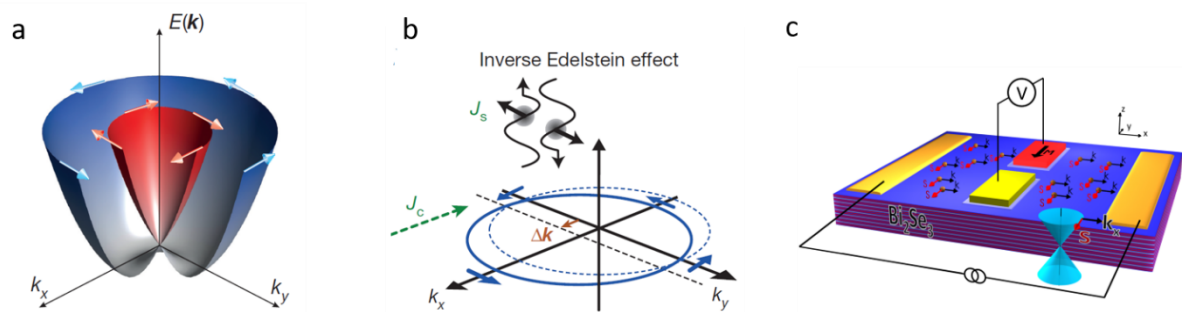


**Figure 5.** Spin-charge conversion in the inversion asymmetry system. a. energy diagram of Rashba system. b. Inverse Edelstein effect. c. spin-momentum locking in topological insulator, $Bi_2Sb_3$.

**Reference**

1.      Kikkawa, T.;   Uchida, K.;   Daimon, S.;   Qiu, Z. Y.;   Shiomi, Y.; Saitoh, E., Critical suppression of spin Seebeck effect by magnetic fields. *Phys Rev B* **2015,** *92* (6).

2.      Pokhodnya, K. I.;   Pejakovic, D.;   Epstein, A. J.; Miller, J. S., Effect of solvent on the magnetic properties of the high-temperature V[TCNE](x) molecule-based magnet. *Phys Rev B* **2001,** *63* (17).

3.      Yoo, J. W.;   Chen, C. Y.;   Jang, H. W.;   Bark, C. W.;   Prigodin, V. N.;   Eom, C. B.; Epstein, A. J., Spin injection/detection using an organic-based magnetic semiconductor. *Nat Mater* **2010,** *9* (8), 638-642.

4.      Liu, H.;   Zhang, C.;   Malissa, H.;   Groesbeck, M.;   Kavand, M.;   McLaughlin, R.;   Jamali, S.;   Hao, J.;   Sun, D.; Davidson, R. A. J. N. m., Organic-based magnon spintronics. *Nat Mater* **2018,** *17* (4), 308.

5.      Yoo, J. W.;   Edelstein, R. S.;   Lincoln, D. M.;   Raju, N. P.;   Xia, C.;   Pokhodnya, K. I.;   Miller, J. S.; Epstein, A. J., Multiple photonic responses in films of organic-based magnetic semiconductor V(TCNE)(x), x similar to 2. *Phys Rev Lett* **2006,** *97* (24).

6.      Ruiz, E.;   Rodríguez-Fortea, A.;   Alvarez, S.; Verdaguer, M. J. C. A. E. J., Is it possible to get high TC magnets with Prussian blue analogues? A theoretical prospect. *Chem. Eur. J.* **2005,** *11* (7), 2135-2144.

7.      Miller, J. S.;   Calabrese, J. C.;   Rommelmann, H.;   Chittipeddi, S. R.;   Zhang, J. H.;   Reiff, W. M.;   Epstein, A. J., Ferromagnetic Behavior of [Fe(C5me5)2]9+[Tcne].-.Structural and Magnetic Characterization of Decamethylferrocenium Tetracyanoethenide, [Fe(C5me5)2].+[Tcne].+.Mecn, and Decamethylferrocenium Pentacyanopropenide, [Fe(C5me5)2].+[C3(Cn)5]-. *Journal of the American Chemical Society* **1987,** *109* (3), 769-781.

8.      Manriquez, J. M.;   Yee, G. T.;   Mclean, R. S.;   Epstein, A. J.; Miller, J. S., A Room-Temperature Molecular Organic Based Magnet. *Science* **1991,** *252* (5011), 1415-1417.

9.      Pokhodnya, K. I.;   Epstein, A. J.; Miller, J. S., Thin-film V[TCNE](x) magnets. *Adv Mater* **2000,** *12* (6), 410-+.

10.      Li, B.;   Zhou, M. Q.;   Lu, Y.;   Kao, C. Y.;   Yoo, J. W.;   Prigodin, V. N.; Epstein, A. J., Effect of organic spacer in an organic spin valve using organic magnetic semiconductor V[TCNE](x). *Org Electron* **2012,** *13* (7), 1261-1265.

11.      Miller, J. S., Organic- and molecule-based magnets. *Mater Today* **2014,** *17* (5), 224-235.

12.      Holmes, S. M.; Girolami, G. S., Sol-gel synthesis of KVII[Cr-III(CN)(6)]center dot 2H(2)O: A crystalline molecule-based magnet with a magnetic ordering temperature above 100 degrees C. *Journal of the American Chemical Society* **1999,** *121* (23), 5593-5594.

13.      Hatlevik, O.;   Buschmann, W. E.;   Zhang, J.;   Manson, J. L.; Miller, J. S., Enhancement of the magnetic ordering temperature and air stability of a mixed valent vanadium hexacyanochromate (III) magnet to 99 degrees C (372 K). *Adv Mater* **1999,** *11* (11), 914-+.

14.      Sato, O.;   Iyoda, T.;   Fujishima, A.; Hashimoto, K., Photoinduced magnetization of a cobalt-iron cyanide. *Science* **1996,** *272* (5262), 704-705.

15.      Sato, O.;   Iyoda, T.;   Fujishima, A.; Hashimoto, K. J. S., Electrochemically tunable magnetic phase transition in a high-Tc chromium cyanide thin film. *Science* **1996,** *271* (5245), 49-51.

16.      Mallah, T.;   Thiebaut, S.;   Verdaguer, M.; Veillet, P., High-T(C) Molecular-Based Magnets - Ferrimagnetic Mixed-Valence Chromium(Iii)-Chromium(Ii) Cyanides with T(C) at 240-Kelvin and 190-Kelvin. *Science* **1993,** *262* (5139), 1554-1557.

17.      Coronado, E.;   Makarewicz, M.;   Prieto-Ruiz, J. P.;   Prima-García, H.; Romero, F. M. J. A. M., Magneto-optical properties of electrodeposited thin films of the molecule-based magnet Cr5. 5 (CN) 12· 11.5 H2O. *Adv. Mater.* **2011,** *23* (37), 4323-4326.

18.      Uchida, K.;   Takahashi, S.;   Harii, K.;   Ieda, J.;   Koshibae, W.;   Ando, K.;   Maekawa, S.; Saitoh, E., Observation of the spin Seebeck effect. *Nature* **2008,** *455* (7214), 778-781.

19.      Uchida, K.;   Xiao, J.;   Adachi, H.;   Ohe, J.;   Takahashi, S.;   Ieda, J.;   Ota, T.;   Kajiwara, Y.;   Umezawa, H.;   Kawai, H.;   Bauer, G. E. W.;   Maekawa, S.; Saitoh, E., Spin Seebeck insulator. *Nat Mater* **2010,** *9* (11), 894-897.

20.      Collet, M.;   de Milly, X.;   d'Allivy Kelly, O.;   Naletov, V. V.;   Bernard, R.;   Bortolotti, P.;   Ben Youssef, J.;   Demidov, V. E.;   Demokritov, S. O.;   Prieto, J. L.;   Munoz, M.;   Cros, V.;   Anane, A.;   de Loubens, G.; Klein, O., Generation of coherent spin-wave modes in yttrium iron garnet microdiscs by spin-orbit torque. *Nat Commun* **2016,** *7*, 10377.

21.      Guo, E. J.;   Cramer, J.;   Kehlberger, A.;   Ferguson, C. A.;   MacLaren, D. A.;   Jakob, G.; Klaui, M., Influence of Thickness and Interface on the Low-Temperature Enhancement of the Spin Seebeck Effect in YIG Films. *Phys Rev X* **2016,** *6* (3), 031012.

22.      Xiao, J.;   Bauer, G. E. W.;   Uchida, K.;   Saitoh, E.; Maekawa, S., Theory of magnon-driven spin

Seebeck effect. *Phys Rev B* **2010,** *81* (21), 214418.

23.      Ritzmann, U.;   Hinzke, D.; Nowak, U., Propagation of thermally induced magnonic spin currents. *Phys Rev B* **2014,** *89* (2), 024409.

24.      Uchida, K.;   Ota, T.;   Adachi, H.;   Xiao, J.;   Nonaka, T.;   Kajiwara, Y.;   Bauer, G. E. W.; Maekawa, S.; Saitoh, E., Thermal spin pumping and magnon-phonon-mediated spin-Seebeck effect. *J Appl Phys* **2012,** *111* (10).

25.      Adachi, H.;   Uchida, K.-i.;   Saitoh, E.;   Ohe, J.-i.;   Takahashi, S.;   Maekawa, S., Gigantic enhancement of spin Seebeck effect by phonon drag. *Appl Phys Lett* **2010,** *97* (25).

26.      Boona, S. R.; Heremans, J. P., Magnon thermal mean free path in yttrium iron garnet. *Phys Rev B* **2014,** *90* (6).

27.      Cornelissen, L. J.;   Liu, J.;   Duine, R. A.;   Ben Youssef, J.; van Wees, B. J., Long-distance transport of magnon spin information in a magnetic insulator at room temperature. *Nat Phys* **2015,** *11* (12), 1022-+.

28.      Valenzuela, S. O.; Tinkham, M., Direct electronic measurement of the spin Hall effect. *Nature* **2006,** *442* (7099), 176-9.

29.      Kimura, T.;   Otani, Y.;   Sato, T.;   Takahashi, S.;   Maekawa, S., Room-temperature reversible spin Hall effect. *Phys Rev Lett* **2007,** *98* (15), 156601.

30.      Sinova, J.;   Valenzuela, S. O.;   Wunderlich, J.;   Back, C. H.; Jungwirth, T., Spin Hall effects. *Rev Mod Phys* **2015,** *87* (4), 1213-1259.

31.      Liu, L. Q.;   Moriyama, T.;   Ralph, D. C.; Buhrman, R. A., Spin-Torque Ferromagnetic Resonance Induced by the Spin Hall Effect. *Phys Rev Lett* **2011,** *106* (3).

32.      Ando, K.;   Takahashi, S.;   Harii, K.;   Sasage, K.;   Ieda, J.;   Maekawa, S.; Saitoh, E., Electric manipulation of spin relaxation using the spin Hall effect. *Phys Rev Lett* **2008,** *101* (3).

33.      Du, C. H.;   Wang, H. L.;   Yang, F. Y.; Hammel, P. C., Systematic variation of spin-orbit coupling with d-orbital filling: Large inverse spin Hall effect in 3d transition metals. *Phys Rev B* **2014,** *90* (14).

34.      Qu, D.;   Huang, S.; Chien, C. J. P. R. B., Inverse spin Hall effect in Cr: Independence of antiferromagnetic ordering. *Phys Rev B* **2015,** *92* (2), 020418.

35.      Jin, M. J.;   Moon, S. Y.;   Park, J.;   Modepalli, V.;   Jo, J.;   Kim, S. I.;   Koo, H. C.;   Min, B. C.; Lee, H. W.;   Baek, S. H.; Yoo, J. W., Nonlocal Spin Diffusion Driven by Giant Spin Hall Effect at Oxide Heterointerfaces. *Nano Lett* **2017,** *17* (1), 36-43.

36.      Choe, D.;   Jin, M. J.;   Kim, S. I.;   Choi, H. J.;   Jo, J.;   Oh, I.;   Park, J.;   Jin, H.;   Koo, H. C.; Min, B. C.;   Hong, S.;   Lee, H. W.;   Baek, S. H.; Yoo, J. W., Gate-tunable giant nonreciprocal charge transport in noncentrosymmetric oxide interfaces. *Nature Communications* **2019,** *10*.

37.      Jiang, Z. L.;   Chang, C. Z.;   Masir, M. R.;   Tang, C.;   Xu, Y. D.;   Moodera, J. S.;   MacDonald, A. H.; Shi, J., Enhanced spin Seebeck effect signal due to spin-momentum locked topological surface states. *Nature Communications* **2016,** *7*.

# Chapter 3. Spin thermoelectric generator in solution-processed YIG/Pt

## 3.1 Motivation

Most of LSSE studies used the yttrium iron garnet ($Y_3F_5O_{12}$, YIG) as a source of spin flow, due mostly to its very low damping of magnetization dynamic and the resulting long spin-wave propagation lifetime [1, 2]. In its bulk crystalline form, YIG is a ferrimagnet with an electronic bandgap of approximately 2.8 eV, so that electronic excitations do not contribute to transport. The antiferromagnetic exchange interaction between $Fe^{3+}$ ions located in two inequivalent sites (two in octahedral and three in tetrahedral environments) leads to a net moment becoming the ferrimagnet. The macroscopic properties of YIG are often described using the typical language of the ferromagnet.

The YIG films have been fabricated by several methods, for example, liquid phase epitaxy (LPE), [3-5] sputtering [6, 7], pulsed laser deposition (PLD) [8-10], and sol-gel method [11-14]. The LSSE with YIG has been studied mostly with the epitaxial YIG film on a gadolinium gallium garnet $Gd_3Ga_5O_{12}$ (GGG) substrate grown by PLD, sputtering, and LPE, which requires highly expensive materials and instruments. In general, the spin pumping with FMR require highly coherent precession motion in need of a monocrystalline FMI layer. But the SSE could largely depend on noncoherent precession motion of magnetic moments excited by thermal energy [15]. Thus, the SSE could be effectively induced even with the polycrystalline film, which can be deposited on various substrates. Further, the magnonic excitation in the polycrystalline YIG could be significantly enhanced because magnetic stiffness will be reduced for higher degree of disorder. The LSSE for the solution processed FMI might have substantially different behavior in its dependence of field, temperature, and thickness of film. Another important factor we need to consider for the LSSE from a solution-processed polycrystalline YIG film is the interface quality. The transfer of a spin current to the neighboring heavy metal layer strongly relies on the spin mixing conductance at the interface [16, 17]. Improving interface quality has been extensively studied for both the epitaxial film and the bulk crystal of YIG. Because the solution-processed film generally has higher degree of roughness, it is critically important to improve interface quality for effective extraction of $E_{ISHE}$ from LSSE. Developing a well-defined solution-processing methodology for the FMI could significantly reduce the energy cost and extend further variety of applications. The solution-process can be easily applied to large-area manufacturing for versatile energy generation. On the other hand, it can also be directly employed on a micro-electronic chip to recycle heat dissipation because it is free from substrate.
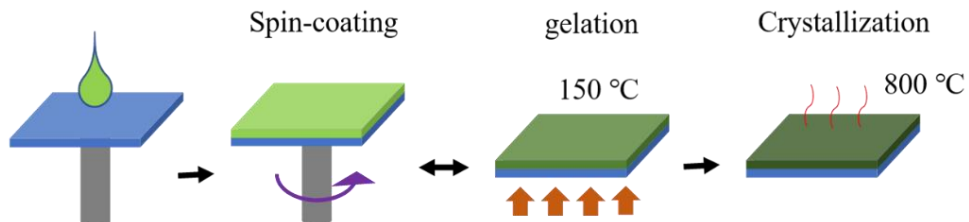
## 3.2 Sample preparation

### 3.2.1 Film fabrication

- • Solution process



M-.S. Jang, JALCOM, **711**, 2017, 693-697

- • Spin-coating & gelation & crystallization



Yttrium nitrate hexahydrate [$Y(NO_3)_3 \cdot 6H_2O$, 99.99% purity] and iron(III) nitrate nonahydrate [$Fe(NO_3)_3 \cdot 9H_2O$, 99.99% purity] powder with a stoichiometric ratio of 3:5 was dissolved in a citric acid ($C_6H_8O_7 \cdot H_2O$). The precursor mixture was dissolved in water (100 mL) and stirred for 24 h at 80 ℃ to obtain a homogeneous solution. The solution was maintained at pH 1. The homogeneous solution was spin-coated on a $SiO_2$ (500 mm) substrate at 4000 rpm for 40 sec.

The film was then baked at 150 ℃ for 3 min to remove residual solvents. To obtain highly homogeneous solution-processed YIG films we used 1 M solution to reduce viscosity. Typical thickness of the spin-coated film was ~ 4 nm. The spin-coating and annealing procedure was repeated for 5 times, which produces typical thickness of the film ~ 20 nm. Lastly, the film was annealed at 800 ℃ for 2 h in an ambient atmosphere. The crystallization of the film was probed by using a high-resolution X-ray diffraction (XRD, D8 ADVANCE, Bruker AXS). The roughness of the film surface was determined by using an atomic force microscopy (AFM, DI-3100, Veeco). The thickness and detailed structure of the stacked film of our LSSE device were further investigated by using a transmission electron microscopy (JEM-2100, JEOL). Magnetic properties of our YIG films were measured by using a superconducting quantum interference device-vibrating sample magnetometer (SQUID-VSM, Quantum Design).

**3.2.2 Solution-processed YIG Film characteristics**

Figure 6 shows the XRD data for the samples with different annealing temperatures. The as-grown YIG film typically undergoes phase transformation with annealing temperature 600 ~ 1000 ℃ depending on the details of environment. Our results showed spin-coated samples with annealing temperature over 800 ℃ become crystallized. The diffraction peaks correspond to (400), (420), and (422) of the YIG film [18, 19]. The strength of diffraction peaks is rather weak due to very thin thickness of the studied YIG film. A cross-section transmission electron microscope (TEM) image of the fabricated device clearly displays a polycrystalline structure of a 20 nm thick YIG film with a well-defined Pt/YIG interface (Figure 7).

Figure 8 shows AFM topography displaying surface roughness of the studied YIG film. One of the obvious disadvantages of the solution-processed YIG film for spin thermoelectric applications is a rough surface because the measured $V_{LSSE}$ (= $E_{ISHE} \times L$) highly depends on an interfacial quality. The thicker YIG film generally induces the higher $V_{LSSE}$, because more number of magnons can be involved in generating a spin current at the YIG/Pt interface. Thus, keeping the thickness of the YIG film and a smooth surface is challenging for the solution-processed YIG film. In this work, we developed the solution-processed polycrystalline YIG thin films which have much lower value of root mean square (RMS) roughness ~ 0.2 nm (for 1×1 mm area) by using a dilute solution. But this process sacrifices the thickness of the YIG film. The obtained RMS of our YIG film is comparable to PLD and LPE deposited epitaxial YIG films.

Figure 9 shows magnetization vs magnetic field measured for our solution processed film. The measurements were done for the magnetic field parallel and perpendicular to the plane of the film. Results show ferromagnetic hysteresis loop with a coercivity about 25 Oe for in-plain magnetic field and 40 Oe for out-of plane magnetic field, respectively. The inset of Figure 9 is a close view of the hysteresis loop. It displays the gradual flip of the magnetization due to the presence of multiple domains in our polycrystalline YIG film. Figure 10 shows the temperature dependent magnetization curve measured for 5 – 300 K. The magnetization monotonically decreases as temperature increases, which could be attributed to the spin wave excitation as well as structural disorder. The inset of Figure 10 displays a plot for the Bloch $T^{3/2}$ law, which describes temperature dependent population of magnons. Deviation from $T^{3/2}$ law can be observed especially at below 100 K. As our polycrystalline YIG films have the discreteness of the lattice and various interaction mechanisms of the spin wave with each other, the magnetization as a function of temperature shows deviation from a standard magnon behavior.
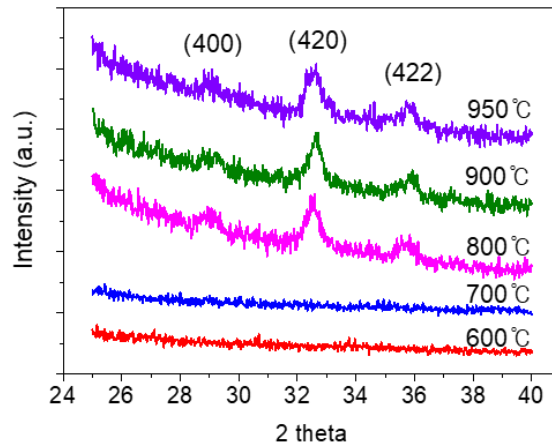
**Figure 6**. The XRD data for the samples with different annealing temperatures. The spin-coated samples are changed by the phase formation with annealing temperature and over 800 °C those films become crystallized and the annealing temperature for the crystallization is a similar result to previous studies [11] [18]. The diffraction peaks correspond to (400), (420), and (422) of the YIG film.[20, 21] The strength of diffraction peaks is rather weak due to very thin thickness of the studied YIG film
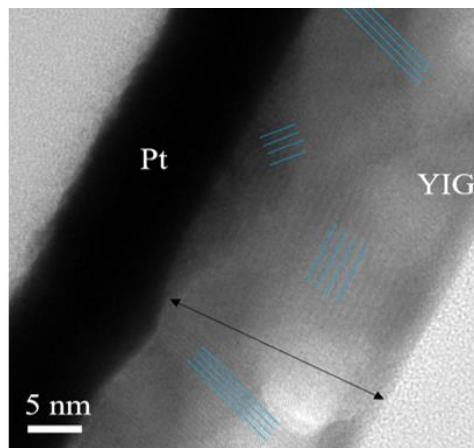


**Figure 7.** TEM image of a Pt (10 nm)/YIG (20 nm) bilayer, which displays polycrystalline nature of the solution-processed YIG film.
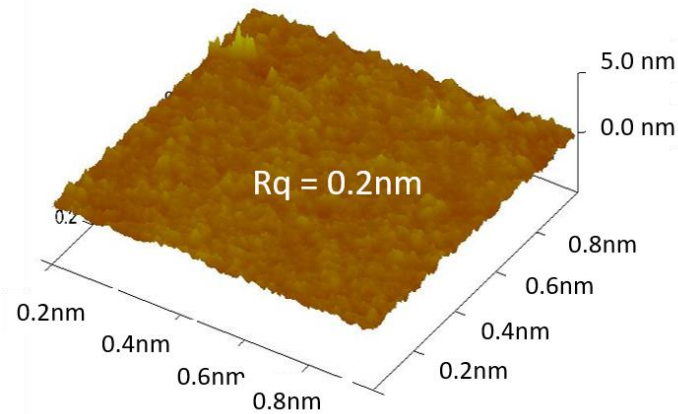
**Figure 8.** An AFM image of the YIG film annealed at 800 °C on the oxidized silicon substrate. The measured rms roughness scanned for 1×1 μm$^2$ area was 0.2 nm.
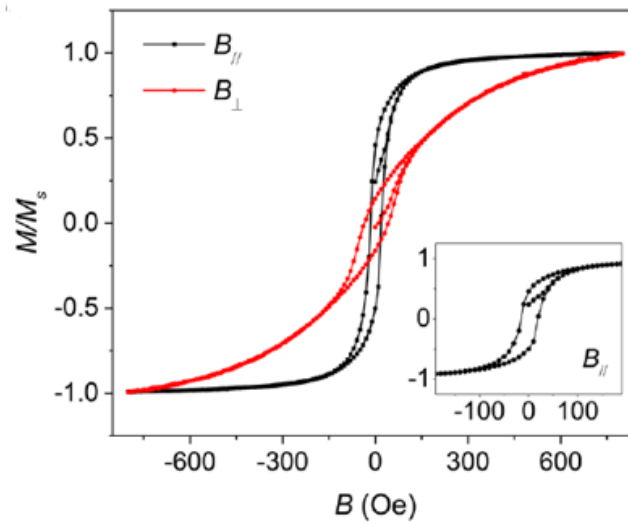


**Figure 9.** Magnetic characteristics of the solution-processed YIG films. Magnetic hysteresis loops measured at 300 K for the applied magnetic fields perpendicular and parallel to the plane of the YIG film.
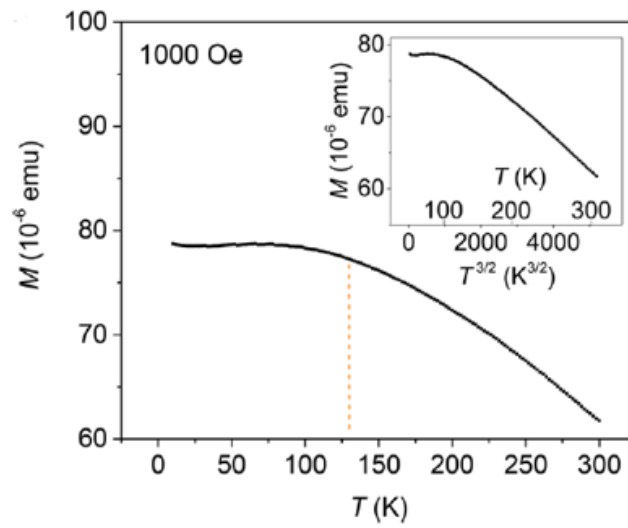
**Figure 10.** Temperature dependence of the magnetization measured for $B = 0.1$ T. Inset displays a plot for the Block's $T^{3/2}$ law of the spin wave.

### 3.2.3 Spin thermoelectric device fabrication

PR coating & soft baking    UV - Exposure    Develop exposed PR

PR

YIG/SiO$_2$/Si

**Pt** E-beam evaporation    PR lift off

Pt    Pt    Repetition for
Heater (Al$_2$O$_3$/Au)
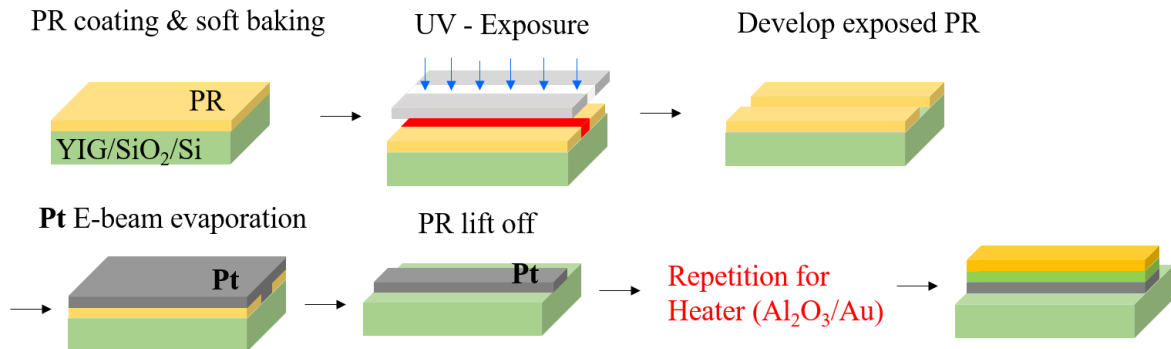
Our LSSE devices have a configuration of Au (30 nm)/Al$_2$O$_3$ (130 nm)/Pt (10 nm)/YIG (20 nm) on oxidized silicon substrates (500 mm). The device patterning was done by using the photo-lithography. The fabricated LSSE devices have a dimension of 200 mm long and 20 mm wide. The Pt film for the detection of LSSE was deposited by the e-beam evaporation under the base presser of ~ 10$^{-7}$ torr. The top Au layer was used for a Joule heating wire to induce heat gradient over the underlying YIG film and simultaneously used for a temperature sensor to calibrate applied temperature gradient. The thick Al$_2$O$_3$ layer was inserted between Au and Pt layers for insulation. Both Al$_2$O$_3$ and Au layers were deposited successively by the e-beam evaporation.

### 3.2.4 Spin thermoelectric device measurements

The current source for the Joule heating was induced by using a Keithley 2636 sourcemeter. The temperature of the Au layer was estimated based on the temperature dependence of the electrical resistivity of the Au layer. Temperature stabilization of the top Au layer depends on the heating current and usually took less than a few min. LSSE measurements were performed 10 min after the temperature of the top Au layer was sufficiently stabilized.

Under the applied temperature gradient, the induced voltage from SSE and ISHE was measured by using a Keithley 2182 nanovoltmeter.  All measurements for LSSE were performed in a physical properties measurement system (PPMS, Quantum Design) with varying temperature and magnetic field.
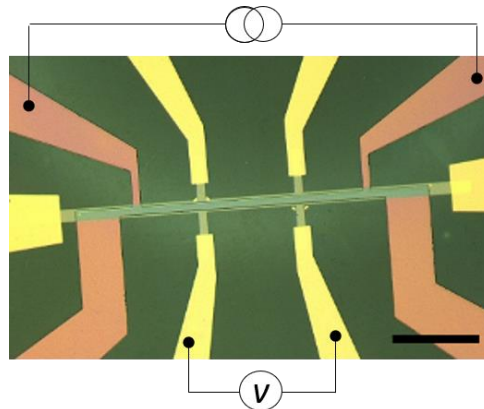


**Figure 11.** The image of the LSSE device. The orange colored electrode represents the top on-chip Au heater for Joule heating. Under the heater, the Pt thin film is connected with Au electrode to detect the ISHE voltage.

## 3.3 Result and discussion

### 3.3.1 Characteristics of the longitudinal spin Seebeck effect

The device consists of a YIG/Pt bilayer for the LSSE spin thermoelectric conversion. The applied longitudinal heat gradient induces magnon excitation and propagation along the vertical direction, which transfers a vertical spin current into the adjacent Pt line. Then, the ISHE generates a transverse electrical voltage along the Pt line.
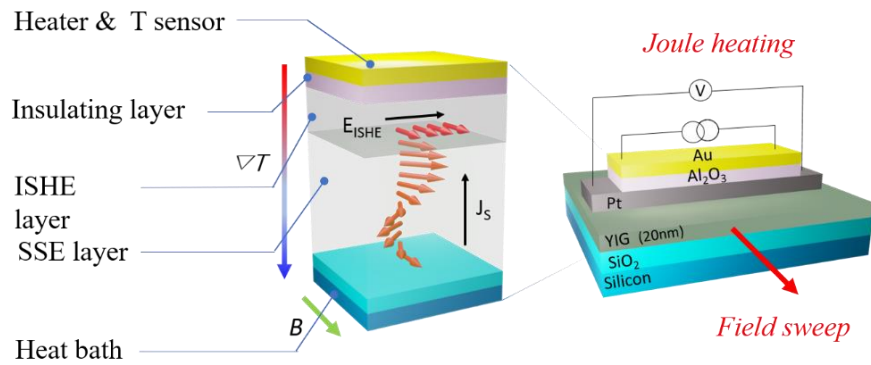


**Figure 12.** Illustration of on-chip heater (Au/Al$_2$O$_3$) device for the measurements of longitudinal spin Seebeck effect. The on-chip heater can be used as a heater and a temperature sensor both.

Schematic of the Figure 12 displays the $V_{\text{LSSE}}$ measurement configuration. Figure 13 shows the obtained LSSE signal for different heating currents in a top Au layer. The on-chip Joule heating can provide a direct thermal contact to the YIG/Pt LSSE device and the precise estimation of the temperature gradient. The temperature gradient was applied from the top gold heating layer to the bottom of the oxidized silicon substrate, which was in thermal contact with a gold plate of a PPMS sample puck. The measurement of $V_{\text{LSSE}}$ was performed while an external magnetic field was swept in the plane of the device. As increasing the heating current through the Au line, significant enhancement of $V_{\text{LSSE}}$ can be observed. The obtained $V_{\text{LSSE}}$ for 40 mA of heating current was around 28 µV. Figure 14 shows variation of resistance of Au, estimated $T_{\text{Au}}$, and measured $V_{\text{LSSE}}$ upon applying currents in the Au heating layer. Because Joule heating power is proportional to $I^2$, temperature of Au layer and the obtained $V_{\text{LSSE}}$ are proportional to $I^2$. To compare the SSE coefficient,

$$S_{\text{LSSE}} = \Delta E_{\text{ISHE}}/\Delta T = (\Delta V_{\text{LSSE}}/L)/(\Delta T/d),$$

quantitatively, we first need to estimate the applied $\Delta T$ on the YIG film. We employed the Fourier's law

$(q_x = -\kappa \frac{dT}{dx})$ of a heat conduction to calculate the temperature gradient, where $\kappa$ is the thermal conductivity of the material. Based on assumption that the heat flux mainly flows through a normal direction, the temperature gradient applied on each layer in the device is proportional to $x/\kappa$. For example, when the applied current was 20 mA, the estimated temperature of the gold layer was 315.43 K based on the change of the resistance of the Au layer. Then, the temperature gradient applied on each layer can be estimated as long as thermal conductivity ($\kappa$) and thickness ($x$) are given. The reference values used for thermal conductivities of Si, SiO$_2$, YIG, Pt, and Al$_2$O$_3$, were 150, 1.4, 8, 72, and 39 W/mK, respectively. Then, the temperature gradient and the spin Seebeck coefficient of the YIG thin film was estimated to be 0.011 K and $S_{\text{LSSE}} \sim 72.8$ nV/K, respectively. Figure 16 displays the measured $V_{\text{LSSE}}$ (= $E_{\text{ISHE}} \times L$) as a function of $\Delta T$ in YIG for the precise estimation of $S_{\text{LSSE}}$. The linear fit produces $V_{\text{LSSE}} / \Delta T \sim 804$ µV/K, which corresponds to $S_{\text{LSSE}} \sim 80.4$ nV/K. The measured spin Seebeck coefficient of our YIG thin film is comparable to what have been reported for thick epitaxial YIG films, [22-26]. In order to clarify the possible artifacts in measured $V_{\text{LSSE}}$ due to leakage or capacitive contributions through the Al$_2$O$_3$, we tested the control sample of Au (30 nm)/ Al$_2$O$_3$ (130 nm)/Pt (10 nm) on oxidized Si substrate, which has the same configuration without the YIG. Results showed that the measured $V_{\text{LSSE}}$ in our solution-processed YIG/Pt devices is originated from LSSE.
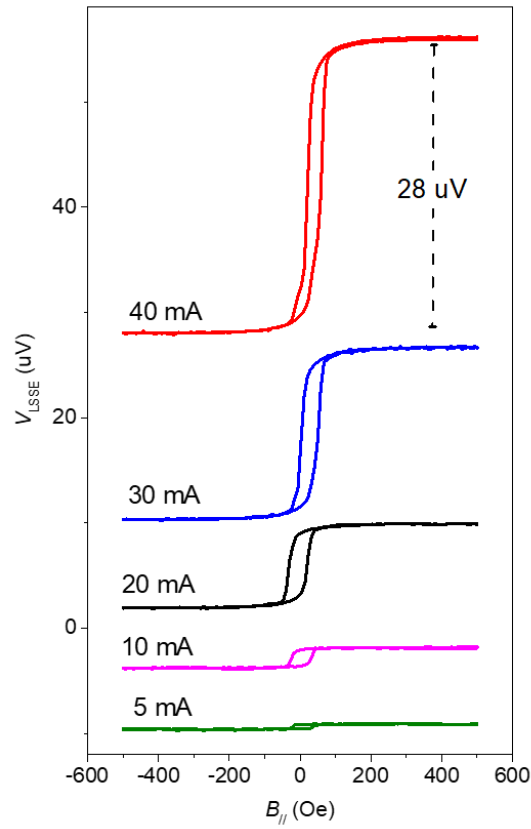
**Figure 13.** LSSE characterization for our solution-processed polycrystalline YIG film. Magnetic field dependent $V_{\text{LSSE}}$ loops at different heating currents.
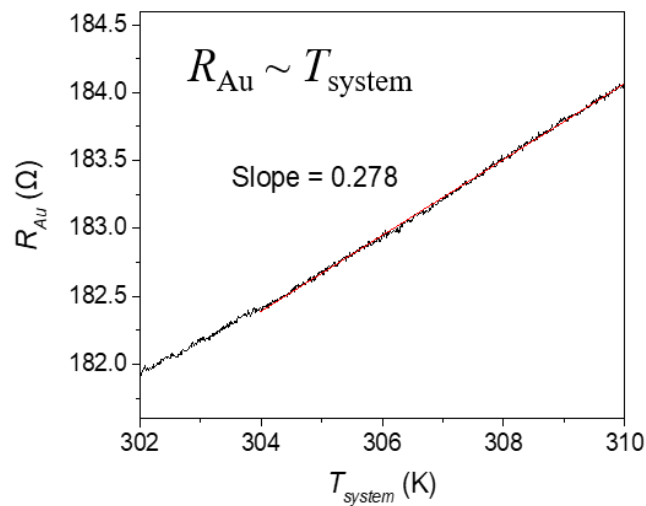


**Figure 14.** Temperature dependent resistance of the Au layer. The red line is the linear fit for temperature dependent resistance slop for the calculation of the Au layer temperature during the Joule heating.
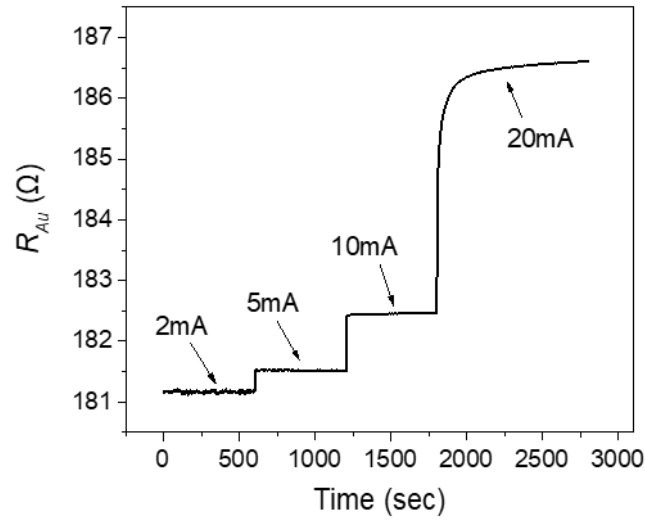
**Figure 15.** The time dependent resistance of the Au film with increasing heating current gradually. The resistance of Au gets to be stable within 10 minutes in low vacuum (~$10^{-2}$ torr).

**Table 1.** Estimated temperature difference of each layer in SSE devices

| | k (W/mK) | Thickness | $\triangle T_{20mA}$ (K) | $\triangle T_{40mA}$ (K) |
|---|---|---|---|---|
| $T_{Au}$-$T_{system}$ | - | - | 15.4 | 51.4 |
| $Al_2O_3$ | 30 | 130nm | 0.015 | 0.063 |
| Pt | 72 | 10nm | 0.0006 | 0.002 |
| YIG | 8 | 20nm | 0.011 | 0.036 |
| $SiO_2$ | 1.4(am.) | 300nm | 0.9 | 3.10 |
| Silicon | 150 | 500um | 14.5 | 48.2 |
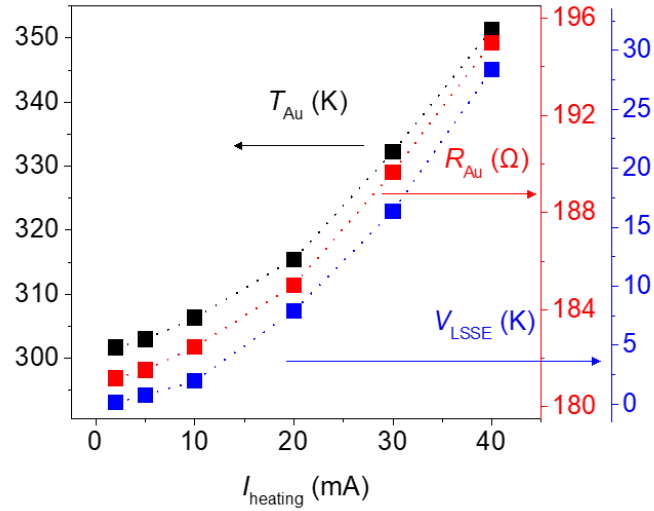
**Figure 16.** The obtained $V_{LSSE}$ (■), resistance of the Au layer (■), and the estimated temperature of the Au layer (■) as a function of the heating current. As the heating current of the Au layer increases, resistance of the Au layer, calculated temperature of the Au layer, and measured $V_{LSSE}$ all increase by $\sim I^2$.

### 3.3.2 Temperature and field dependent longitudinal spin Seebeck effect

The $V_{LSSE}$ depending on a system temperature was measured by sweeping the magnetic field at each fixed temperature as shown in the Figure 17. The applied current to the Au heating line was 20 mA. The measured $V_{LSSE} = V(+H) - V(-H)$ is about 7.9 mV at 300 K. The VLSSE increases gradually with lowering temperature and exhibits a peak at around 110 K. Then, it starts to decrease as temperature decreases further. In general, the temperature dependence of $V_{LSSE}$ highly rely on the magnon excitation and propagation [24]. The excitation of magnon and its population follows Bloch $T^{3/2}$ law. Thus, less number of magnons involve in SSE at lower temperature. However, the propagation length of magnon increases as temperature decreases. Thus, LSSE is often described by an atomistic spin model, $V_{LSSE} \propto 1 - \exp(-L/\xi)$ [23, 27], where $\xi$ is the characteristic length of the magnon and $L$ is the thickness of the sample. Increasing thickness of a YIG film allows more number of magnons involved in LSSE induced spin current generation at the Pt/YIG interface until the thickness of the YIG film becomes comparable to

the propagation length of magnon. The estimated value of $\xi$ for the epitaxial YIG film from the literatures is around ~ 1 mm at room temperature and it monotonically increases as temperature is lowered [24]. Thus, $V_{\text{LSSE}}$ from the epitaxial YIG film with thickness around several mm increases as temperature is lowered from room temperature and shows maximum at the temperature, where the size effect starts to dominate magnon scattering. Then, it decreases as temperature is lowered further due to the reduced excitation of magnon at very low temperature. The temperature dependence of our YIG film also displays similar behavior. But it should not be correlated with the characteristic length of magnon because our solution-processed YIG film has thickness much less than $\xi$ at all temperature. Thus, the mechanism of LSSE in the solution-processed thin YIG film would be affected by other factors. The propagation of phonon can also significantly affect SSE through two different mechanisms. One is the phonon-mediated process in the YIG film. The phonon-mediated non-equilibrium drives thermal spin pumping, which leads to strong enhancement of SSE at low temperature following the temperature dependent thermal conductivity of YIG. However, it was reported that the polycrystalline YIG film displayed negligible low temperature enhancement of SSE [28]. Another mechanism that can induce strong enhancement of SSE at low temperature is phonon-drag at the interface between the YIG film and the substrate.54 This effect is effective for the transverse configuration of SSE producing extremely long magnon propagation length55. But such phonon-drag effects become negligible for the longitudinal configuration of SSE [29]. It is because the phonon transport in the substrate and magnon transport in the YIG film occurs in series in the longitudinal configuration while the two processes take place in parallel for the transverse configuration. The substrate phonon-drag effect could be effective in our studies because our solution-processed YIG films are extremely thin compared to YIG films used for other LSSE studies. The thermal non-equilibrium from the substrate could continuously drive magnon excitation and propagation in our thin YIG film leading to a relatively high value of $S_{\text{LSSE}}$.

**Figure 17.** Temperature dependence of LSSE signals for a Joule heating current of the top gold layer $I_{heating}$ = 20 mA. Measurements were done with sweeping magnetic field between -500 and 500 Oe.
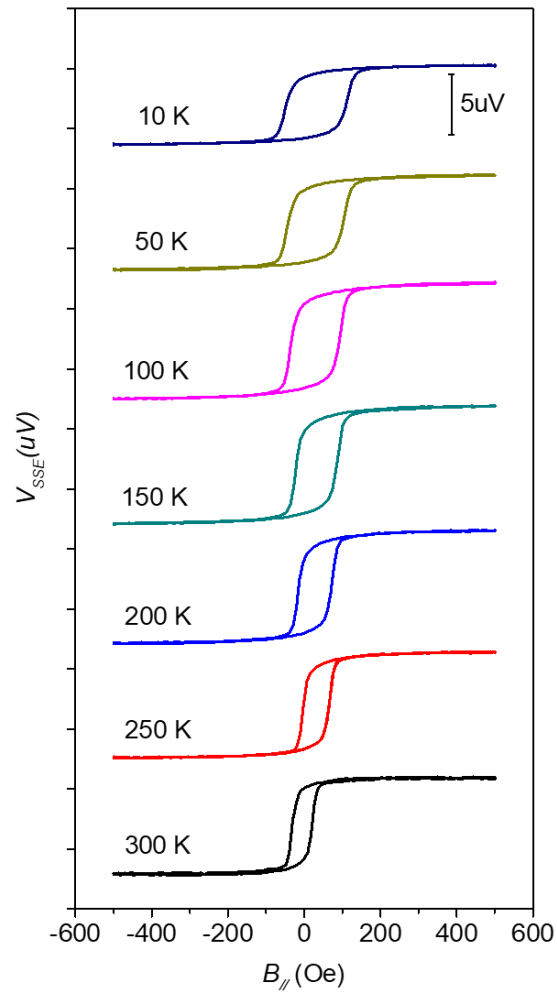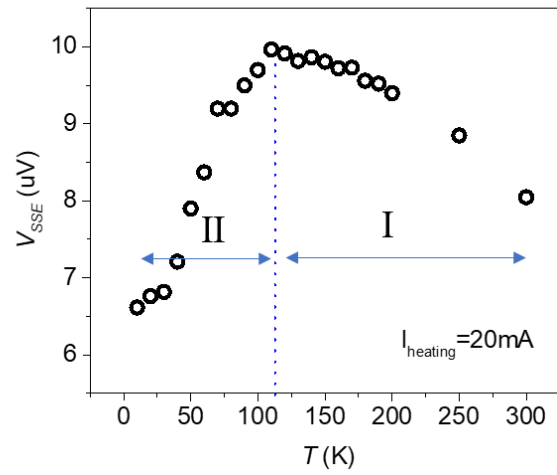
**Figure 18.** Temperature dependence of LSSE signals for a Joule heating current of the top gold layer $I_{\text{heating}}$ = 20 mA. Temperature dependent saturated LSSE signals which is calculated by $\Delta V_{\text{LSSE}} = [V_{\text{LSSE}}$ ($+H_y$) - $V_{\text{LSSE}}$ (-$H_y$)].

Figure 19 displays magnetic field dependence of $V_{\text{LSSE}}$ measured at 300 K with 20 mA heating current. For a thick YIG film, high magnetic field generally suppresses $V_{\text{LSSE}}$ due to the suppression of long wavelength magnon excitations [24]. If the thickness of the YIG film is less than the characteristic length $\xi$, high field suppression disappears. The high magnetic field dependence of $V_{\text{LSSE}}$ in our device is shown in Figure 19. The observed $V_{\text{LSSE}}$ even increases as the magnetic field increases. This behavior might be attributed to the polycrystalline nature of our solution-processed film because magnetization of our YIG film gradually increases with increasing field due to multi-domain structure and magnetic anisotropy. Behavior of LSSE in a polycrystalline YIG is substantially different from that of epitaxial film, which requires further exploration.



**Figure 19.** Magnetic field dependent LSSE signals measured at 300 K for $I_{\text{heating}} = 20$ mA.

42

## 3.4 Conclusion

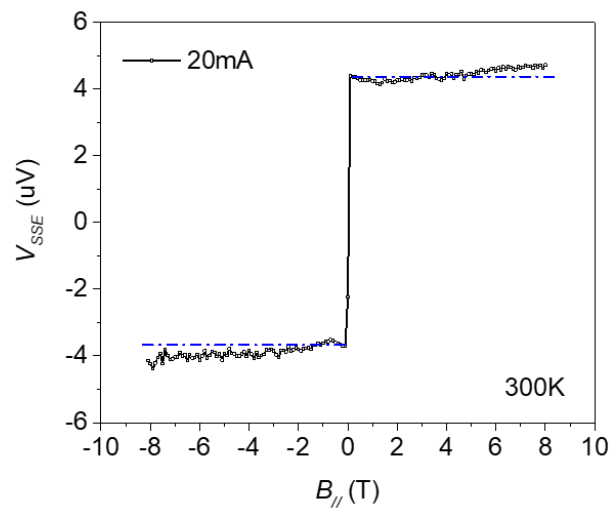A highly uniform solution-processed YIG film was fabricated by facile method and the LSSE was investigated experimentally by the on-chip microelectronic spin Seebeck devices. The solution-processed 20 nm thick YIG film with a 10 nm Pt film were used for the spin Seebeck energy converter. The top Au layer was used for a heater to induce a vertical temperature gradient as well as for a temperature sensor. The roughness of a YIG film was reduced to 0.2 nm by simply diluting precursor solution, which sacrifices the thickness of a spin-coated film. In general, thicker YIG films induce higher LSSE voltage because a greater number of magnons can be involved in transferring the spin current at the interface of a YIG/Pt bilayer. As a result, the estimated spin Seebeck coefficient for our micro-electronic device is $S_{\mathrm{LSSE}} \sim 80.4$ nV/K. This value is comparable to the typical reported values for thick epitaxial YIG films. Temperature dependence of LSSE voltage in our devices suggests effective phonon-drag invigorates thermal spin-pumping. And magnetic field dependent behavior of SSE reflects noncoherent magnon excitations due to higher degree of disorder. The demonstrated effective LSSE with solution-processed thin YIG films can be applied for a verity of substrates leading to ubiquitous spin thermoelectric power generations.

# Reference

1. Collet, M.; de Milly, X.; d'Allivy Kelly, O.; Naletov, V. V.; Bernard, R.; Bortolotti, P.; Ben Youssef, J.; Demidov, V. E.; Demokritov, S. O.; Prieto, J. L.; Munoz, M.; Cros, V.; Anane, A.; de Loubens, G.; Klein, O., Generation of coherent spin-wave modes in yttrium iron garnet microdiscs by spin-orbit torque. *Nat Commun* **2016,** *7*, 10377.

2. Jungfleisch, M. B.; Chumak, A. V.; Kehlberger, A.; Lauer, V.; Kim, D. H.; Onbasli, M. C.; Ross, C. A.; Klaui, M.; Hillebrands, B., Thickness and power dependence of the spin-pumping effect in Y3Fe5O12/Pt heterostructures measured by the inverse spin Hall effect. *Phys Rev B* **2015,** *91* (13).

3. Pirro, P.; Brächer, T.; Chumak, A. V.; Lägel, B.; Dubs, C.; Surzhenko, O.; Görnert, P.; Leven, B.; Hillebrands, B., Spin-wave excitation and propagation in microstructured waveguides of yttrium iron garnet/Pt bilayers. *Applied Physics Letters* **2014,** *104* (1).

4. Cornelissen, L. J.; van Wees, B. J., Magnetic field dependence of the magnon spin diffusion length in the magnetic insulator yttrium iron garnet. *Physical Review B* **2016,** *93* (2).

5. Dubs, C.; Surzhenko, O.; Linke, R.; Danilewsky, A.; Brückner, U.; Dellith, J., Sub-micrometer yttrium iron garnet LPE films with low ferromagnetic resonance losses. *Journal of Physics D: Applied Physics* **2017,** *50* (20).

6. Houchen, C.; Peng, L.; Wei, Z.; Tao, L.; Hoffmann, A.; Longjiang, D.; Mingzhong, W., Nanometer-Thick Yttrium Iron Garnet Films With Extremely Low Damping. *IEEE Magnetics Letters* **2014,** *5*, 1-4.

7. Lustikova, J.; Shiomi, Y.; Qiu, Z.; Kikkawa, T.; Iguchi, R.; Uchida, K.; Saitoh, E., Spin current generation from sputtered Y3Fe5O12 films. *Journal of Applied Physics* **2014,** *116* (15).

8. Sun, Y.; Song, Y.-Y.; Chang, H.; Kabatek, M.; Jantz, M.; Schneider, W.; Wu, M.; Schultheiss, H.; Hoffmann, A., Growth and ferromagnetic resonance properties of nanometer-thick yttrium iron garnet films. *Applied Physics Letters* **2012,** *101* (15).

9. Onbasli, M. C.; Kehlberger, A.; Kim, D. H.; Jakob, G.; Kläui, M.; Chumak, A. V.; Hillebrands, B.; Ross, C. A., Pulsed laser deposition of epitaxial yttrium iron garnet films with low Gilbert damping and bulk-like magnetization. *APL Materials* **2014,** *2* (10).

10. d'Allivy Kelly, O.; Anane, A.; Bernard, R.; Ben Youssef, J.; Hahn, C.; Molpeceres, A. H.; Carretero, C.; Jacquet, E.; Deranlot, C.; Bortolotti, P.; Lebourgeois, R.; Mage, J. C.; de Loubens, G.; Klein, O.; Cros, V.; Fert, A., Inverse spin Hall effect in nanometer-thick yttrium iron garnet/Pt system. *Appl Phys Lett* **2013,** *103* (8).

11. Minqiang, W.; Xiangying, Z.; Xiaoyong, W.; Liangying, Z.; Xi, Y., Preparation and annealing process of Y3Fe5O12by sol-gel method. *Ferroelectrics* **2001,** *264* (1), 249-254.

12. Guo, X.; Chen, Y.; Wang, G.; Zhang, Y.; Ge, J.; Tang, X.; Ponchel, F.; Rémiens, D.; Dong, X., Growth and characterization of yttrium iron garnet films on Si substrates by Chemical Solution Deposition (CSD) technique. *Journal of Alloys and Compounds* **2016,** *671*, 234-237.

13. Hirata, S.; Ono, T.; Amemiya, Y.; Tabei, T.; Yokoyama, S., Influence of surface smoothing on spin Seebeck effect of Ce1Y2Fe5O12 deposited by metal organic decomposition. *Japanese Journal of Applied Physics* **2017,** *56* (4S).

14. Musa, M. A.; Azis, R. a. S.; Osman, N. H.; Hassan, J.; Zangina, T., Structural and magnetic properties of yttrium iron garnet (YIG) and yttrium aluminum iron garnet (YAlG) nanoferrite via sol-gel synthesis. *Results in Physics* **2017,** *7*, 1135-1142.

15. Chang, F.-J.; Lin, J. G.; Huang, S.-Y., Robust spin current generated by the spin Seebeck effect. *Physical Review Materials* **2017,** *1* (3).

16. Qiu, Z.; Ando, K.; Uchida, K.; Kajiwara, Y.; Takahashi, R.; Nakayama, H.; An, T.; Fujikawa, Y.; Saitoh, E., Spin mixing conductance at a well-controlled platinum/yttrium iron garnet interface. *Applied Physics Letters* **2013,** *103* (9).

17. Qiu, Z.; Hou, D.; Uchida, K.; Saitoh, E., Influence of interface condition on spin-Seebeck effects. *Journal of Physics D: Applied Physics* **2015,** *48* (16).

18. Jang, M.-S.; Roh, I.-J.; Park, J.; Kang, C.-Y.; Choi, W. J.; Baek, S.-H.; Park, S. S.; Yoo, J.-W.; Lee, K.-S., Dramatic enhancement of the saturation magnetization of a sol-gel synthesized Y 3 Fe 5 O 12 by a mechanical pressing process. *Journal of Alloys and Compounds* **2017,** *711*, 693-697.

19. Dongquoc, V.; Kuchi, R.; Van, P. C.; Yoon, S.-G.; Jeong, J.-R., Effects of heating rate on the magneto-optical properties of bismuth-substituted yttrium iron garnet films prepared via modified metal-organic decomposition. *Current Applied Physics* **2018,** *18* (2), 241-245.

20. Jang, M. S.; Roh, I. J.; Park, J.; Kang, C. Y.; Choi, W. J.; Baek, S. H.; Park, S. S.; Yoo, J.

W.; Lee, K. S., Dramatic Dramatic enhancement of the saturation magnetization of a sol-gel synthesized Y3Fe5O12 by a mechanical pressing process. *J. Alloys. Compd.* **2017,** *711*, 693-697.

21.      Dongquoc, V.;  Kuchi, R.;  Van, P. C.;  Yoon, S. G.; Jeong, J. R., Effects of heating rate on the magneto-optical properties of bismuth-substituted yttrium iron garnet films prepared via modified metal-organic decomposition. *Current Applied Physics* **2018,** *18* (2), 241-245.

22.      Uchida, K.;  Adachi, H.;  Ota, T.;  Nakayama, H.;  Maekawa, S.; Saitoh, E., Observation of longitudinal spin-Seebeck effect in magnetic insulators. *Appl Phys Lett* **2010,** *97* (17), 172505.

23.      Kehlberger, A.;  Ritzmann, U.;  Hinzke, D.;  Guo, E. J.;  Cramer, J.;  Jakob, G.;  Onbasli, M. C.; Kim, D. H.;  Ross, C. A.;  Jungfleisch, M. B.;  Hillebrands, B.;  Nowak, U.; Klaui, M., Length Scale of the Spin Seebeck Effect. *Phys Rev Lett* **2015,** *115* (9), 096602.

24.      Guo, E. J.;  Cramer, J.;  Kehlberger, A.;  Ferguson, C. A.;  MacLaren, D. A.;  Jakob, G.; Klaui, M., Influence of Thickness and Interface on the Low-Temperature Enhancement of the Spin Seebeck Effect in YIG Films. *Phys Rev X* **2016,** *6* (3), 031012.

25.      Sola, A.;  Bougiatioti, P.;  Kuepferling, M.;  Meier, D.;  Reiss, G.;  Pasquale, M.;  Kuschel, T.; Basso, V., Longitudinal spin Seebeck coefficient: heat flux vs. temperature difference method. *Sci Rep* **2017,** *7*, 46752.

26.      Yuasa, H.;  Nakata, F.;  Nakamura, R.; Kurokawa, Y., Spin Seebeck coefficient enhancement by using Ta50W50 alloy and YIG/Ru interface. *Journal of Physics D: Applied Physics* **2018,** *51* (13).

27.      Ritzmann, U.;  Hinzke, D.; Nowak, U., Propagation of thermally induced magnonic spin currents. *Phys Rev B* **2014,** *89* (2).

28.      Uchida, K.;  Ota, T.;  Adachi, H.;  Xiao, J.;  Nonaka, T.;  Kajiwara, Y.;  Bauer, G. E. W.; Maekawa, S.; Saitoh, E., Thermal spin pumping and magnon-phonon-mediated spin-Seebeck effect. *J Appl Phys* **2012,** *111* (10).

29.      Adachi, H.;  Uchida, K.-i.;  Saitoh, E.;  Ohe, J.-i.;  Takahashi, S.; Maekawa, S., Gigantic enhancement of spin Seebeck effect by phonon drag. *Appl Phys Lett* **2010,** *97* (25).

# Chapter 4. STE in Molecule-based magnet

## 4.1 Motivation

Several inorganic magnetic insulators have been used for STE devices demonstrating effective spin thermoelectric energy conversion [1, 2]. In particular, YIG has been most widely used for STE applications because its low Gilbert damping constant ($\alpha = 2.3 \times 10^{-4}$) [3, 4] allows long distance magnon propagation. However, inorganic magnetic insulator films are inappropriate for practical STE applications due to scaling problem, as they are difficult to grow into large area and require high temperature processing for crystallization [5, 6]. On the other hand, organic- and/or molecular films are generally grown at lower temperature. And their flexible synthetic route endows scalable deposition technique. Moreover, organic-based magnetic film, vanadium tetracyanoethylene ($V[TCNE]_{x\sim 2}$) has shown effective spin-polarized carrier injection [7, 8] as well as coherent magnon generation and spin pumping [9].



● $M^1$　● $M^2$　⧗ -CN-
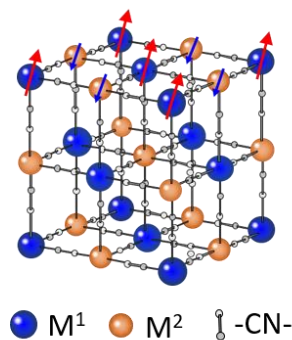
Prussian blue analogue is another family of molecule-based magnets having a molecular formula of $AM^1[M^2(CN)_6]x \cdot nH_2O$ (A is alkali cation, $M^1$ and $M^2$ are transition metal ions). The magnetic interaction between spins in nearest transition ions is mediated through $\pi$ orbitals in CN bridges. Substitution of transition metals at $M^1$ and $M^2$ sites can produce wide range of a magnetic transition temperature. For example, $Cr^{II}[Cr^{III}(CN)_6]x \cdot nH_2O$ (Cr-PBA) showed $T_c$ up to 240 K [10-12] and $V^{II}[Cr^{III}(CN)_6]x \cdot nH_2O$ powder exhibited $T_c$ up to 376 K [13-15]. Thus, this class of magnets could be utilized for alternative magnetic insulator in the STE device with an advantage of versatile synthesis amenable for large area deposition at room temperature. In addition, the molecule-based magnet may present weak spin-orbit coupling and lack of spin-lattice scatterings, relevant features for effective propagation of thermally exited magnons.

## 4.2 Sample preparation

### 4.2.1 Electrochemical deposition of Cr-PBA film on Cr layer
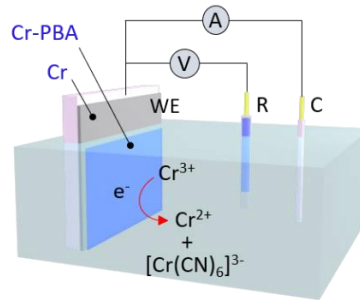


For the deposition of $Cr^{II}[Cr^{III}(CN)_6]$ Prussian blue analogue (Cr-PBA) films, we employed an electrochemical deposition (ECD) method, which can be easily adopted for large-area-, low-cost-, and mass-production of thin films. In order to build a STE bilayer device, a magnetic insulator needs to be grown on a thin metallic film carrying a high spin Hall angle for the effective spin-charge conversion from the magnon-delivered spin angular moments. However, heavy metals such as Pt, Pd are not appropriate for the working electrode due to hydrogen generation by electrolysis of water at the reduction voltage of $Cr^{3+}$ ($E = -0.88$ V vs Ag/AgCl reference electrode). A Cr metal does not display hydrogen generation during ECD, and it has spin Hall angle comparable to those of heavy metals such as Pt, W, Pd. Thus, we adapted a Cr thin film (10 nm) as a working electrode, which was deposited on $SiO_2$ (300 nm)/$p$-Si (500 mm) substrate by thermal evaporation at high vacuum ($\sim 7x10^{-7}$ Torr). The aqueous solution mixed with 5 mM $K_3Cr(CN)_6$ and 7.5 mM $CrCl_3 \cdot H_2O$ was stirred for 30 min at room temperature in order to sufficiently dissolve the reagents in water (HPLC grade). The Cr-PBA film was grown at a fixed potential (E = $-0.88$ V vs Ag/AgCl reference electrode) using Pt counter electrode. Typical cyclic voltammetry curves are displayed in Fig 19a. Fig. 19b exhibits recorded static current generated during the deposition of Cr-PBA. After the deposition, samples were rinsed with water and dried with $N_2$ gas. The film thickness was determined by using a surface profiler (P-6 stylus profiler, KLA Tencor). For the sample of 600 sec ECD deposition, average thickness was $\sim 1.4$ mm.
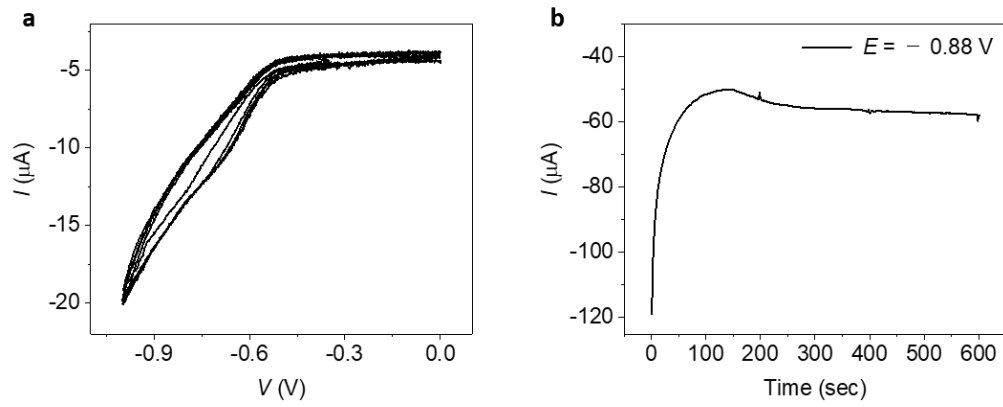
**Figure 20. Electrochemical deposition of Cr-PBA in an aqueous solution. a,** Cyclic voltammetry curve for the observation of reductive reaction from $0.0$ V into $-1.0$ V. **b,** The generated current recorded for 10 minutes during the deposition of the Cr-PBA film at $E = -0.88$ V.

48

### 4.2.2 Spin thermoelectric device fabrication

We used a heterojunction of Au (20 nm)/Al$_2$O$_3$ (130 nm)/Parylene (400 nm)/Cr-PBA (1.4 mm)/Cr (10 nm) for the characterization of LSSE in Cr-PBA/Cr STE device. After deposition of Cr-PBA on the Cr film, 400 nm of parylene was deposited to protect the entire sample by using a standard parylene coater (Alpha plus). For the fabrication of the studied device, the reactive ion etching was done with O$_2$ and Cl$_2$ gas by using thick photoresist (AZ9660) as a protective buffer patterned for a dimension of 5 mm length and 100 mm width. After removing the buffer photoresist by acetone, the additional insulating layer of Al$_2$O$_3$ (130 nm) and the top Au heater (20 nm) patterned into the same dimension of Cr-PBA (5 mm length and 100 mm width) were successively deposited by e-beam evaporation
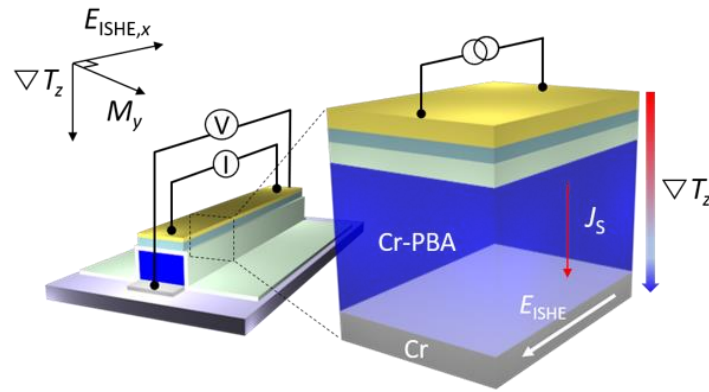


**Figure 21.** A schematic illustration for the LSSE characterization of the Cr-PBA/Cr STE device. The temperature gradient was applied by Joule heating of a top Au line. The vertical flow of magnons pumps a pure spin current to the adjacent Cr layer. Then, the induced spin flow is converted into a longitudinal charge current producing electric field of $E_{ISHE}$.

### 4.2.3 Thermal conductivity device fabrication

To determine the thermal conductivity of the Cr-PBA film, we adopted the differential 3ω method [16]. As shown in figure 22, we deposited a Cr-PBA film (4 mm) on the half of the Cr (10 nm) /*p*-Si substrate. Then, the thin insulating layer of parylene C was coated by using a parylene coater (Alpha plus). Thickness of the parylene layer was about 400 nm, guaranteeing electrical isolation of the gold heater to function as a thermometer. In this way, the sample (Parylene/Cr-PBA/Cr/*p*-Si) and the reference (Parylene/Cr/*p*-Si) were fabricated on the same substrate. Then, 20 mm x 500 mm gold heater lines were patterned on top of both sides of the sample and reference sample parts.
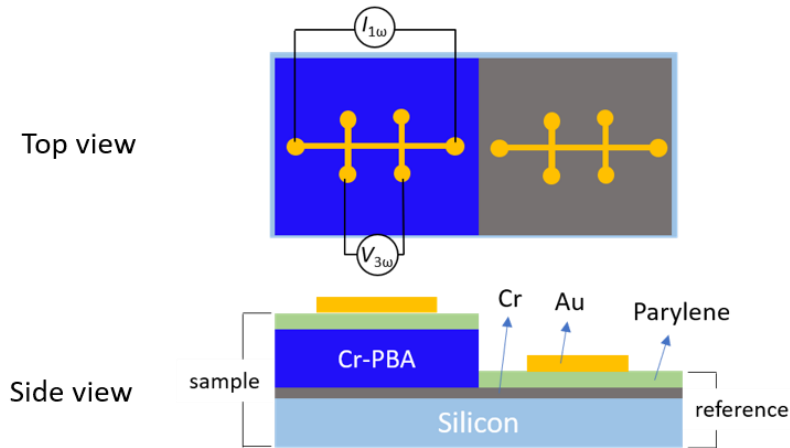


**Figure 22.** Schematic illustration of top and cross-section view for the thermal conductivity measurement sample and the reference which are fabricated on the same substrate.

## 4.3 Result and discussion

### 4.3.1 Cr-PBA film characteristics

Surface morphology was probed by atomic force microscopy (AFM). The obtained rms roughness of the film surface was 6.78 nm and 14.3 nm for 1×1 mm and 5×5 mm area, respectively (Fig 22). A cross-sectional transmission electron microscope (TEM) image of the developed Cr-PBA/Cr heterojunction is shown in Fig. 23 displaying sharp interface. X-ray diffraction (XRD) spectra of the ECD deposited Cr-PBA films are shown in Fig. 24. XRD spectra of Cr-PBA films with deposition time of 600 and 1200 sec, which are 1.4 and 2.5 μm thick, respectively. Results confirm a fcc phase of PBA with main peaks 24.2 (220), 34.5 (400), 38.7 (420), and 52.8 (600) [17].



**Figure 23. AFM images of the Cr-PBA film surface.** The estimated roughness of the Cr-PBA film is 6.78 nm and 14.3 nm for 1×1 mm and 5×5 mm area, respectively.



**Figure 24.** The cross-sectional TEM image of a Cr-PBA/Cr bilayer deposited on an oxidized silicon substrate

**Figure 25.** XRD spectra of Cr-PBA films with deposition time of 600 and 1200 sec, which are 1.4 and 2.5 mm thick, respectively. Results confirm a fcc phase of PBA with main peaks 24.2 (220), 34.5 (400), 38.7 (420), and 52.8 (600)
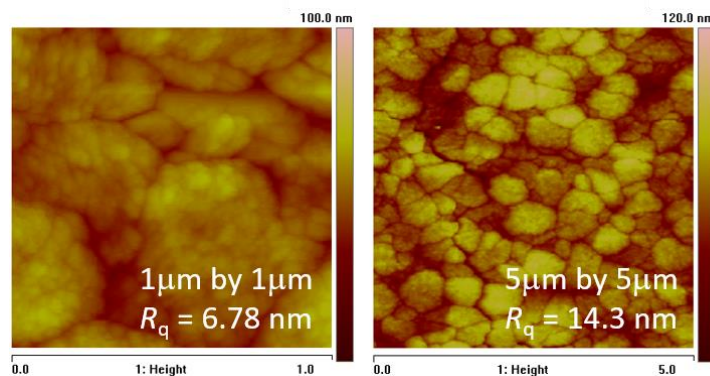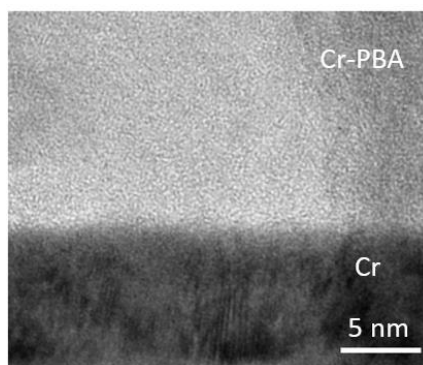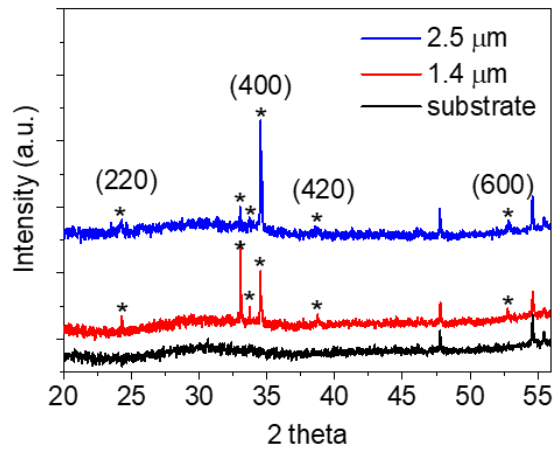
### 4.3.2 Magnetic properties of Cr-PBA

The magnetic hysteresis of the ECD deposited Cr-PBA film exhibits a coercivity of ~ 25 Oe for in-plane applied magnetic field at 100 K as shown in Fig. 25. The temperature-dependent magnetization curve is displayed in Fig. 26. The estimated transition temperature $T_c$ ~ 223 K, which is close to $T_c$ ~ 240 K of the crystalline powder [10]. This discrepancy is likely due to a slight change in the stoichiometric ratio between $Cr^{2+}$ ($S = 2$) and $Cr^{3+}$ ($S = 2/3$), as it changes net spin numbers, variations of crystal field, and the strength of superexchange coupling [18]. In the Fig. 27, the strong monotonic increase of magnetization with decreasing temperature reflects active excitations of magnons as it follows Block $T^{3/2}$ law Weak suppression of magnetization at very low temperature would be attributed to the reentrance behavior due to non-uniform stoichiometry of the deposited film.

The magnetic characteristic of the ECD deposited Cr-PBA film was studied by using SQUID-VSM (Quantum Design) immediately after the deposition. Magnetic hysteresis of the Cr-PBA film measured for in-plane applied magnetic field at 100 K exhibits a coercivity of about 25 Oe as shown in Fig. 25. The gradual flip of the magnetization shows polycrystalline characteristic of the Cr-PBA film. In order to examine the stability of sample, we measured magnetic hysteresis of Cr-PBA after keeping the sample for one month in an ambient air. We did not observe any discernible change in magnetization. The temperature dependent magnetization measured at 10 Oe is displayed in Fig 26. Dashed sky-blue line is a fit by using the mean-field theory of ferromagnetic phase transition, $(T−T_c)^{\beta}$. The obtained transition temperature $T_c$ is about 223 K, which is close to $T_c$ ~ 240 K of the crystalline powder samples. The temperature-dependent magnetization curves exhibit typical behavior of temperature dependent magnon excitation. Fig 27 displays plots for the Bloch $T^{3/2}$ law displaying a good linearity over the wide range of temperature.  Fitting with $M(T) = M_0(1−aT^{3/2})$ provides the value of slope ~ $2.6×10^{-4}$ $K^{-3/2}$. This value of slope is much higher than that of Ni ($7.5×10^{-6}$ $K^{-3/2}$) [19]. Thus, the excitations of magnons with low wave vectors are more effective in our Cr-PBA film. This behavior indicates strong suppression of sub-thermal magnons at high magnetic field, which is consistent with the strong suppression of the $V_{LSSE}$ at high magnetic field. Weak suppression of magnetization at very low temperature would be attributed to the reentrance behavior due to non-uniform stoichiometry of the deposited film. In the Fig 28, the strong bifurcation between zero field cool (ZFC) and field cool (FC) magnetization suggests spin glass like behavior of Cr-PBA film.

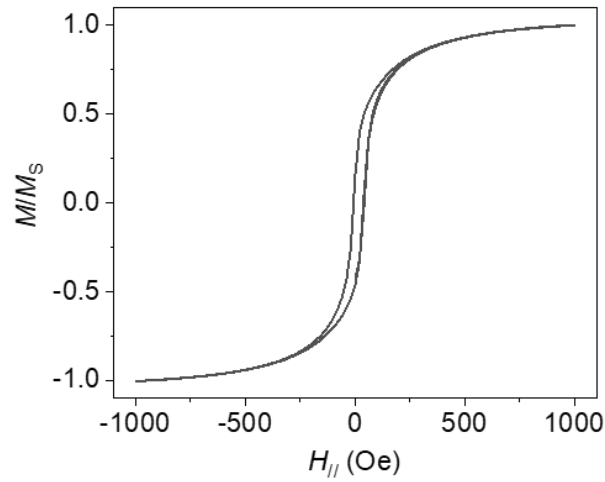**Figure 26.** The magnetic hysteresis curve of the ECD deposited Cr-PBA film measured for in-plane applied magnetic field at 100 K.



**Figure 27. Temperature dependent magnetization of the ECD Cr-PBA film.** The magnetization as function of temperature from 2 K to 300 K measured with in-plane magnetic field of 10 Oe. Fitting with the mean-field theory $\sim (T_c\text{-}T)^{\beta}$ produces $T_c \sim 223$ K.

**Figure 28. Plot of the Block $T^{3/2}$ law.** The temperature dependent saturation magnetization as a function of $T^{3/2}$ displaying a good linearity over the wide range of temperature. Measurement was done with applying magnetic field of $H = 0.5$T. Fitting with $M(T) = M_0(1-aT^{3/2})$ provides the value of slope ~ $2.6 \times 10^{-4}$ K$^{-3/2}$, which is much higher than those of inorganic magnets.



**Figure 29. Spin glass behavior of the Cr-PBA film.** The temperature dependent magnetization measured for zero-field-cooled (ZFC) and field-cooled (FC) sample in applied magnetic field of 100 Oe. The strong bifurcation between ZFC and FC reflects spin glass-like behavior due to non-uniform stoichiometry of Cr-PBA film.

### 4.3.3 Thermal conductivity of Cr-PBA

The 3ω method is useful way for measuring a film thermal conductivity as well as bulk materials. To measure a thermal conductivity by the method, a thin conductive layer is needed on a specimen as a heater and temperature sensor. The principle of 3ω method is that the generated heat from the heater is diffused into the specimen and the thermal wave diffusion is detected by AC voltage and calculated into the penetration depth. The equation of t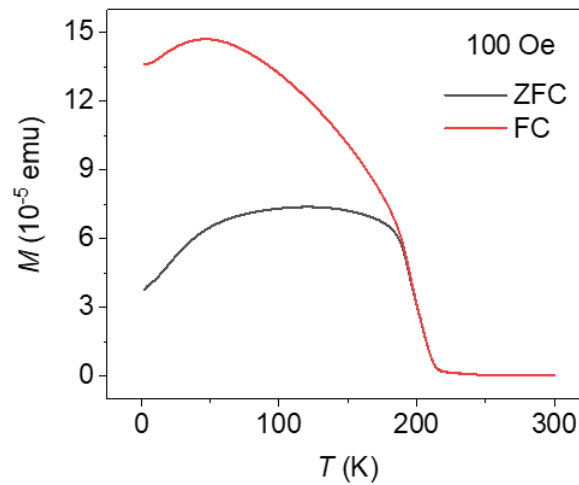he thermal conductivity by this method is obtained by D. G. Cahill and R. O. Pohl [20]. Thus, we can calculate the thermal conductivity of a specimen with simple following equation.

$$\kappa = \frac{V^3 ln\frac{f_1}{f_2}}{4\pi l R^2 (V_{3,1} - V_{3,2})}\frac{dR}{dT}$$

where, $f$ is frequency, $V_{3,1}$ and $V_{3,2}$ is third harmonic voltage at $f_1$, $f_2$ respectively, $V$ is first harmonic voltage, and $R$ is average resistance of the heater line, $dR/dT$ is the slop of temperature dependent resistance.

To determine the thermal conductivity of our Cr-PBA film we adopted differential 3ω measurements. It is useful when we have several layer accumulated samples or have to attain cross-plane and in-plane thermal conductivity [16]. For our devices, since the Cr-PBA is deposited on the Cr metal and is covered by parylene, differential 3ω method is needed to calculate the thermal conductivity of Cr-PBA. The third harmonic voltage ($V_{3\omega}$) and the first harmonic voltage ($V_{1\omega}$) enable to determine the cross-sectional temperature drop ($\Delta T$) from the relation,

$$\Delta T = 2R\frac{dT}{dR}\frac{V_{3\omega}}{V_{1\omega}},$$

where $R$ is the resistance of a Au heater line. Fig 21 displays estimated cross-sectional temperature drop in the sample and reference, respectively. The difference of temperature drop between sample and reference indicates an exclusive temperature drop across the Cr-PBA film ($\Delta T_{film}$). For the heater power ($P$) of 7.2 mW, the estimated $\Delta T_{film}$ is ~ 2.47 K. Then, the thermal conductivity of the film can be determined by the following equation,

$$\kappa = P{\cdot}d_f/(w_h l_h{\cdot}\Delta T_{film})$$

where $d_f$, $w_h$, and $l_h$ are the thickness of the film, the width and length of the Au heater, respectively. The thermal conductivity of the Cr-PBA film was estimated to be 1.17 W/mK, when the applied heating power was 7.2 mW. We repeated measurements with increasing the applied heater power as shown in
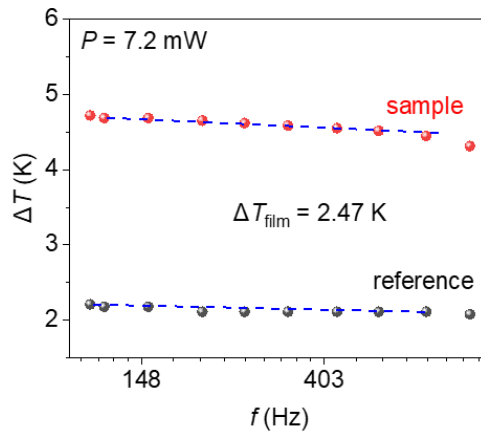
**Figure 30. Differential 3ω measurements for the determination of the thermal conductivity of the Cr-PBA film.** 2ω oscillation (ΔT) as a function of logarithm frequency. Both the sample and reference display nearly the same linearity. The difference of the temperature (ΔT$_{film}$) is calculated to be 2.47 K.
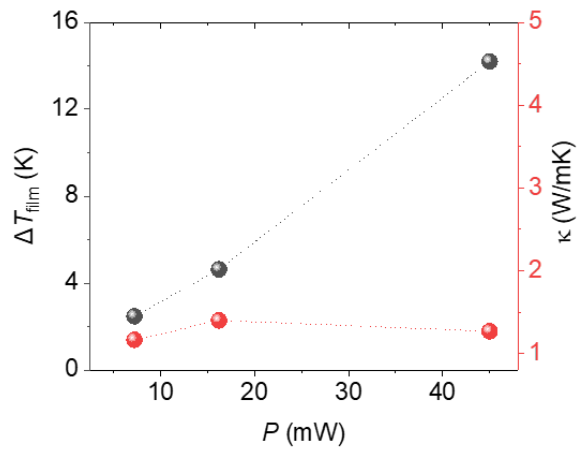


**Figure 31.** Estimated ΔT$_{film}$ (black circle) and the thermal conductivity (red circle) as increasing the heater power.

**4.3.4 Spin thermoelectric observation of Cr-PBA/Cr hybrid heterostructure**

For the characterization of spin thermoelectricity of the developed heterojunction devices, a heat gradient was applied by Joule heating of a Au line on top of the device as shown in figure 21. The on-chip Au line was also used simultaneously as a temperature sensor. An electrical insulation between the top Au heater and Cr-PBA/Cr bilayer was done by the insertion of $Al_2O_3$ (130 nm)/Parylene (400 nm) films. The bottom of a device substrate (Si) was in thermal contact with a gold plate of a physical properties measurement system (PPMS) sample puck to maintain vertical temperature gradient. The applied heat gradient by the Au heater generates vertical directional propagation of magnons in the magnetic insulator Cr-PBA. Then, this magnonic spin flow pumps a spin current in the adjacent Cr film, where it is converted into a charge current generating $V_{LSSE}$. Figure 32 shows the measured LSSE signals ($V_{LSSE}$) as a function of $zy$ angle of the applied magnetic field (1 T). $V_{LSSE}$ exhibits a sinusoidal behavior with maximum magnitude when $H$ and $\nabla T_z$ are perpendicular each other because it is proportional to $J_s \times \sigma$. Fig. 32 shows $V_{LSSE}$ as a function of applied $H_y$ measured for different $I_{heater}$. $V_{LSSE}$ exhibits weak hysteresis behavior and nearly saturates at around 3 kOe. With increasing $I_{heater}$, $V_{LSSE}$ also increases. The obtained $\Delta V_{LSSE}$ [$\Delta V_{LSSE} = V(5 \text{ kOe}) - V(-5 \text{ kOe})$] for $I_{heater} = 20$ mA was 47.3 μV.



**Figure 32.** $V_{LSSE}$ as a function of $zy$ angle of the applied magnetic field (1 T) at 100 K. Measurements were done for the Cr-PBA (1.4    m)/Cr (10 nm) STE device. $V_{LSSE}$ upon sweeping the applied magnetic field measured with different heating currents $I_{heater} = 10, 15,$ and 20 mA at 100 K.
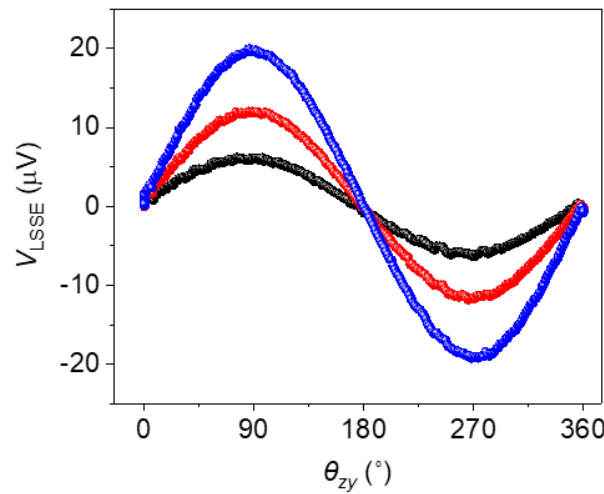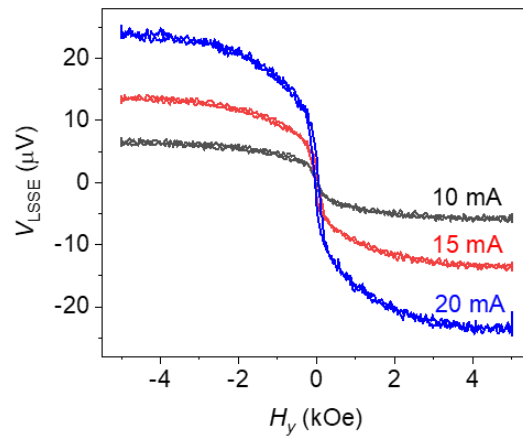
**Figure 33** $V_{LSSE}$ as a function of *zy* angle of the applied magnetic field (1 T) at 100 K. Measurements were done for the Cr-PBA (1.4 m)/Cr (10 nm) STE device. $V_{LSSE}$ upon sweeping the applied magnetic field measured with different heating currents $I_{heater}$ = 10, 15, and 20 mA at 100 K.

### 4.3.5 Temperature calibration of top heater

To estimate the spin Seebeck coefficient ($S_{LSSE}$) of our STE devices, a temperature gradient applied on the Cr-PBA film need to be obtained. We employed the top Au heating layer as an in-situ temperature sensor. Thus, heat loss at the interface between a STE device and a temperature sensor can be ignored allowing precise calibration of temperature. The measurements were conducted in a PPMS chamber under precise control of the system-temperature. Bottom of the substrate of the STE device was attached to the gold plate of the PPMS sample puck with a thermal M grease. The temperature of the top Au layer was estimated based on the temperature dependent resistance of the Au layer. Fig. 34 displays temperature dependent resistance of the Au layer. The slope of the *R-T* curve is 0.363 ($\Omega$/K). The measurement was done with source current, 0.1 mA, to exclude Joule heating. Fig. 35 displays the time dependent resistance of the Au layer during heating with stepwise currents. As the heating current was increased in step, the resistance of the Au layer was also increased stepwise. The resistance of the Au line was immediately stabilized without suffering an oscillation because the heating power of the micro-scale Au wire is not high enough to affect the system temperature of the PPMS. For the applied current of 10 mA, a temperature stabilization takes less than min. The temperature of the top Au heater for the heating current of 15 mA is estimated to be 104.91 K.
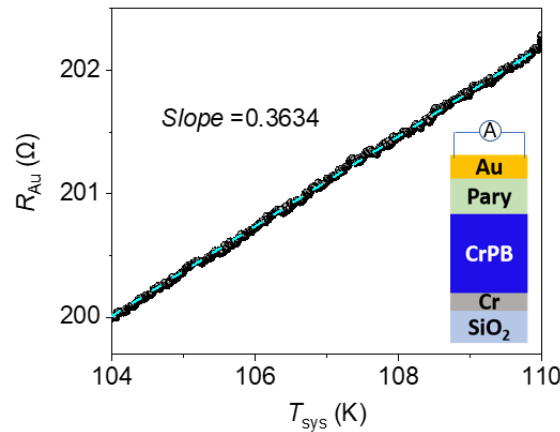


**Figure 34 Temperature calibration using the on-chip Au heater line.** The temperature dependent resistance of the Au heater recorded for the calibration of the temperature at the top Au layer.
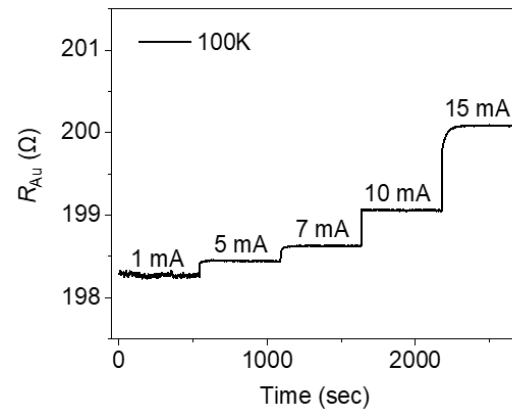
**Figure 35.** The resistance of the Au line recorded during the stepwise increase of a Joule heating current at 100 K.

### 4.3.6 Calculation of Temperature gradient for Cr-PBA film

We then calculated the temperature gradient applied in each layer by using the Fourier's Law,

$$q_x = -\kappa A \frac{dT}{dx},$$

where $q_x$, $\kappa$, $A$ are the heat flux (W), thermal conductivity (W/mK), and surface area, respectively. Thus, the temperature difference applied on each layer will be proportional to $d/\kappa$, where $d$ is the thickness of each layer. The reference values of $\kappa$ are used for the thermal conductivity of each layer except the Cr-PBA layer. The unknown thermal conductivity of Cr-PBA was obtained based-on the differential 3ω method. The calculated temperature difference on each layer for various heating currents is summarized in Table 1. Fig. 36 illustrates the temperature gradient applied in each layer of our STE device for a heating current of 15 mA.

To characterize the spin Seebeck coefficient ($S_{\text{LSSE}}$) of our STE devices, we measured the thermal conductivity ($\kappa$) of a Cr-PBA film based on a differential 3ω method [21, 22]. Then, the estimation of the applied temperature gradient in each layer of our STE device was done by employing the Fourier's law ($q_x = -\kappa \frac{dT}{dx}$) of a heat conduction. Details of temperature calibration are described in Fig. 36 and Table 2.

**Table 2.** The calculated temperature difference applied in each layer. The temperature difference applied in each layer can be calculated by the heat flux relation between thickness and thermal conductivity ($\Delta T \sim d/\kappa$).

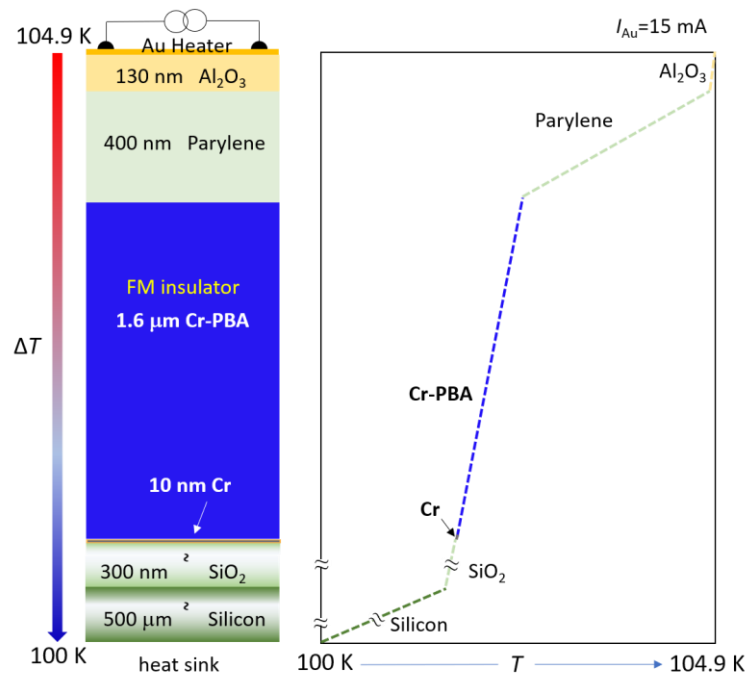| | $\kappa$ (W/mK) | Thickness | $\triangle T_{10mA}$ | $\triangle T_{15mA}$ | $\triangle T_{20mA}$ |
|---|---|---|---|---|---|
| $T_{Au}$-$T_{system}$ | | 20 nm | 2.16 K | 4.91 K | 10.18 K |
| $Al_2O_3$ | 30 | 130 nm | 0.00098 K | 0.0022 K | 0.0046 K |
| Parylene | 0.082 | 400 nm | 1.1 K | 2.5 K | 5.2 K |
| **Cr-PBA** | 1.28 | 1.4 μm | **0.25 K** | **0.56 K** | **1.17 K** |
| Cr | 93.9 | 10 nm | 0.000024 K | 0.000055 K | 0.00011 K |
| $SiO_2$ | 1.4 | 300 nm | 0.049 K | 0.11 K | 0.23 K |
| Si | 150 | 500 μm | 0.76 K | 1.72 K | 3.57 K |



**Figure 36. Schematic illustration of the temperature gradient in the STE device.** The schematic figure of the temperature gradient in each layer of the STE device. The smaller the thermal conductivity is, the higher temperature gradient occurs. The studied STE device has the highest temperature gradient on the parylene layer, followed by the Cr-PBA film.

### 4.3.7 Characteristics of LSSE in Cr-PBA/Cr hybrid heterostructure

The obtained LSSE signal for different heating currents ($I_{heater}$) in the on-chip Au heater can provide precise estimation of the LSSE coefficient. Because the heat flux is generated by Joule heating, the resistance of the Au heater ($R_{Au}$), the temperature difference applied in Cr-PBA ($\Delta T_{Cr\text{-}PBA}$) and the obtained $V_{LSSE}$ are proportional to $\sim I_2$ as shown in Fig 37. Then, the spin Seebeck coefficient, defined as $S_{LSSE} = E_{ISHE}/\nabla T = (\Delta V_{LSSE}/L)/(\Delta T_{Cr\text{-}PBA}/d)$ (where $L$ is the interval between voltage probes and $d$ is the thickness of the Cr-PBA film), can be estimated from the slope of $\Delta V_{LSSE}/\Delta T_{Cr\text{-}PBA}$. The obtained spin Seebeck coefficient of the Cr-PBA/Cr device at 100 K was $S_{LSSE} = 11.1$ nV/K. The observed $\Delta V_{LSSE}$ can be also induced from other effects associated with heating. Anomalous Nernst effect (ANE) has been considered as one of the main sources to contribute $V_{LSSE}$, because proximity induced magnetism at the interface could induce heat gradient induced voltage with the same spatial symmetry with $V_{LSSE}$. Thus, we measured anomalous Hall effect (AHE) to investigate a proximity effect in our heterojunction (Fig. 39). The hall bar structure was patterned to measure Hall voltage ($V_{xy}$). We applied 1 mA of source currents to exclude Joule heating during the Hall measurements. Result show the absence of a proximity effect in the Cr layer (Fig. 39). Thus, the observed $V_{LSSE}$ in our device is not associated with ANE and mainly originates from LSSE. We also tested magneto-resistance (MR) of the Au and Cr layer to confirm parasite effect that may contribute to the observed $V_{LSSE}$, especially in high magnetic field (Fig. 40). For the measurement of MR in the Cr layer, we applied from 1 mA to 100 mA to exclude Joule heating and applied the external magnetic field up to 7 T. The observed resistance change at high magnetic field was less than 0.043 %. For the Au heater line, we measured MR by applying 10 mA to examine heating variation as increasing magnetic field. The change of resistance was less than 0.037 %, which does not contribute to the significant variation in $V_{LSSE}$ at high magnetic field as shown in Fig. 40.
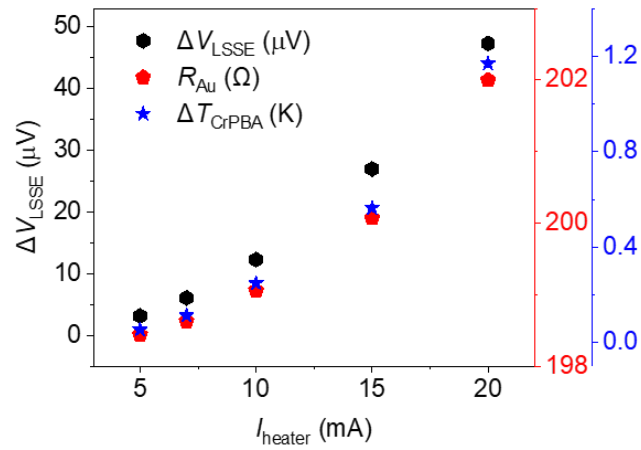
**Figure 37 Heating power dependence.** $\Delta V_{LSSE}$ (black circles), resistance of the Au layer ($R_{Au}$, red pentagon), and the temperature difference in Cr-PBA ($\Delta T_{Cr-PBA}$, blue stars) measured with increasing the heating current at 100 K.
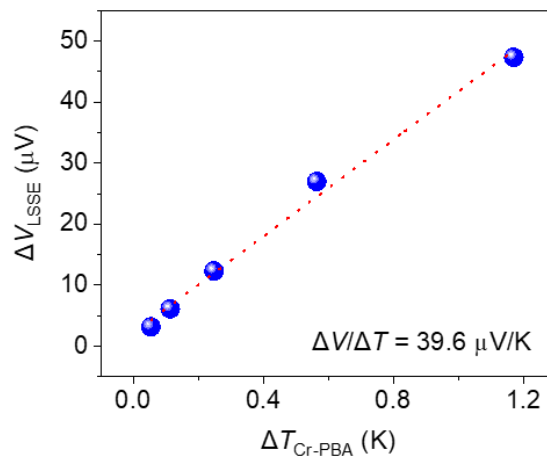


**Figure 38.** $\Delta V_{LSSE}$ as a function of the estimated $\Delta T$ in a Cr-PBA film displaying a linear behavior. The obtained value of the slope is $\Delta V_{LSSE}/\Delta T$ is ~ 39.6 mV/K

**Figure 39. Anomalous Hall effect in the Cr-PBA/Cr heterojunction.** The observed $V_{LSSE}$ is often involved with an experimental artifact from the anomalous Hall effect (AHE) because the proximity effect could induce spontaneous magnetization in Cr layer. The AHE was measured with standard Hall geometry of the Cr-PBA/Cr bilayer at 100 K. Results clearly display absence of AHE.
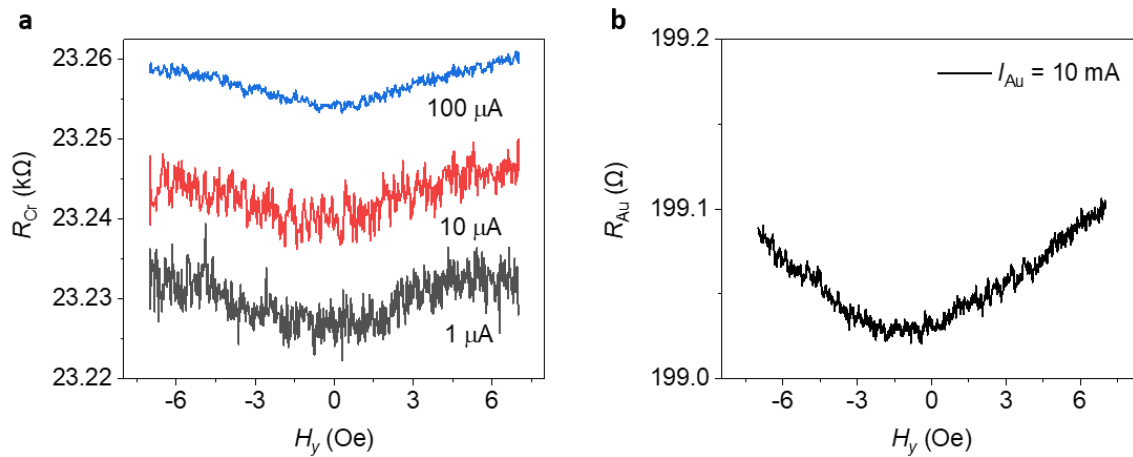


**Figure 40. MRs under the applied field $H_y$.** The MRs of the Cr layer (a) and the top Au heater line (b) measured for the applied in-plane magnetic field ($H_y$). Results display negligible MRs in both Cr and Au electrodes. Thus, MRs of the electrodes have negligible effect in the calibration of the measured $V_{LSSE}$.

**4.3.8 Temperature and magnetic field dependence of STE conversion of Cr-PBA/Cr hybrid heterostructure**

Figure 41 displays $V_{LSSE} (H_y)$ measured at various temperatures. $\Delta V_{LSSE}$, defined as $V_{LSSE} (+H_y) - V_{LSSE} (-H_y)$ at $H_y = 5$ kOe, as a function of temperature is plotted in Fig. 42. As increasing temperature, the $\Delta V_{LSSE}$ initially increases gradually and then, it starts to decrease after exhibiting a peak at around 60 K. The maximum $\Delta V_{LSSE}/\Delta T \sim 59.6$ μV (at 60 K). In the LSSE configuration, the temperature dependence of $\Delta V_{LSSE}$ relies on the magnon excitation and its vertical propagation in the thin film of a magnetic insulator. As temperature decreases, the number of excited magnons gradually decrease following Bloch $T^{3/2}$ law but the magnon characteristic length ($\xi$) significantly increases. Within the atomic spin model, the measured $\Delta V_{LSSE}$ is proportional to $1 - \exp(-d/\xi)$, where $d$ is the thickness of the magnet [23]. Thus, increase of $\xi$ with lowering $T$ leads to enhancement of $\Delta V_{LSSE}$ because more number of magnons involve in spin pumping at lower temperature. In our Cr-PBA film, $\xi$ becomes comparable to the thickness of the film below 60 K. This size effect together with Block $T^{3/2}$ law lead to the decrease of $\Delta V_{LSSE}$ below 60 K. Figure 43 displays the high magnetic field dependence of $\Delta V_{LSSE}$. As the magnetic field increases, the LSSE signal monotonically suppressed. The ratio of $\Delta V_{LSSE}$ change at 7 T, $[(V_{LSSE} (0.5$ T$)-V_{LSSE} (7$ T$))/V_{LSSE} (0.5$ T$)]\times 100$ %, was calculated to be 47 %, which is significantly higher than those of typical inorganic magnetic insulators. The changes of resistance in the Au heater line and the Cr layer in high-magnetic field are negligible and not associated with high-field suppression of $\Delta V_{LSSE}$. The high field suppression of $\Delta V_{LSSE}$ can be attributed to the suppression of sub-thermal magnons[24]. Fig. 27 displays a plot for the Bloch $T^{3/2}$ law exhibiting a good linearity over the wide range of temperature. Fitting with $M(T) = M_0(1-aT^{3/2})$ provides the value of slope $a \sim 2.6\times 10^{-4}$ K$^{-3/2}$. This value of slope is much higher than those of Ni ($7.5\times 10^{-6}$ K$^{-3/2}$) [19] and NiFe$_2$O$_4$ ($4\times 10^{-5}$ K$^{-3/2}$) [25]. Thus, the excitations of magnons with low wave vectors are more effective in our Cr-PBA film. This behavior indicates strong suppression of sub-thermal magnons will occur at high magnetic field, which is consistent with the strong suppression of the $V_{LSSE}$ at high magnetic field, shown in Figure 43. This feature is highly beneficial for collecting electricity from the applied heat gradient in magnet.
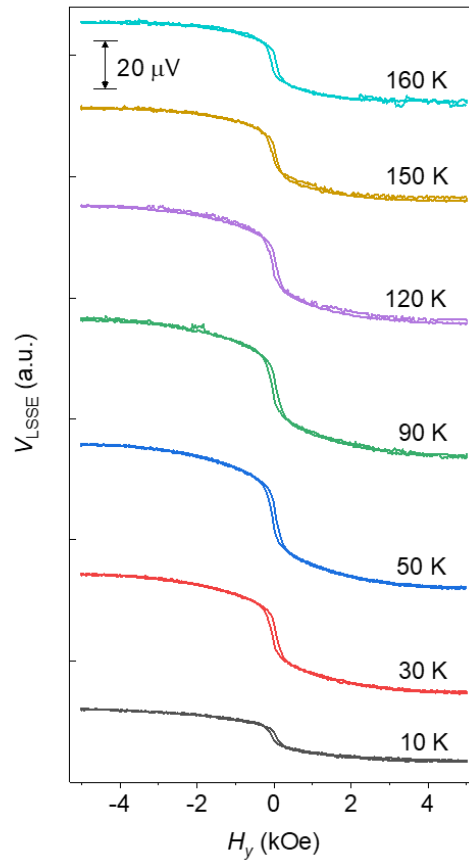
**Figure 41.** Temperature dependence of $V_{LSSE}$ measured with a Joule heating current, $I_{heater}$ = 20 mA ($\Delta T_{Cr\text{-}PBA}$ = 1.17 K). Measurements were done for the Cr-PBA (1.4 μm)/Cr (10 nm) STE device with sweeping magnetic field ($H_y$) between –5 kOe and 5 kOe. $V_{LSSE}$ ($H_y$) curves are vertically shifted for clarity.
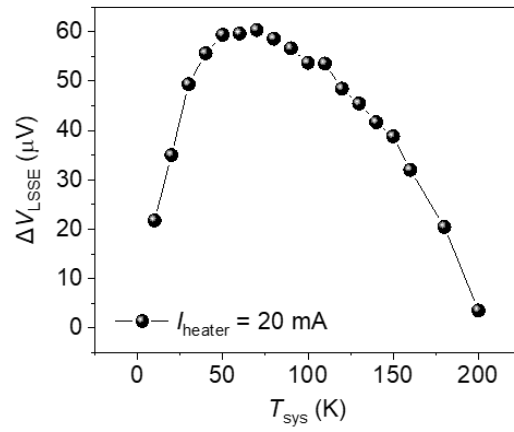
**Figure 42** Temperature dependence of $\Delta V_{LSSE} = [V_{LSSE}(+H_y) - V_{LSSE}(-H_y)]$ ($H_y$ = 5 kOe), displaying a peak at around 60 K.
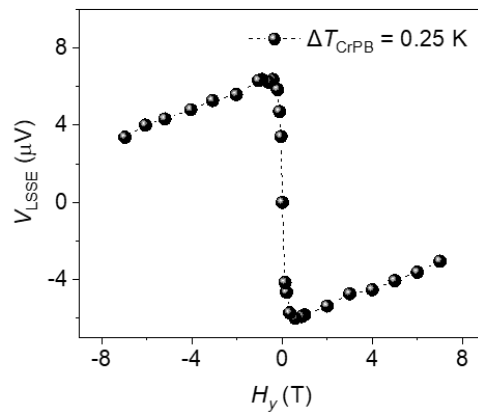


**Figure 43**. High magnetic field-dependence of $V_{LSSE}$ measured at 100 K with $I_{heater}$ = 10 mA ($\Delta T_{Cr-PBA}$ = 0.25 K).

## 4.1 Conclusion

I introduced a new class of magnetic materials for spin-thermoelectric energy conversion with promising performance for various spin-caloritronic applications. The employed molecular magnetic films carry a number of advantages over inorganic magnetic insulators thanks to flexible film fabrication processing, which allows low-temperature-, large-area-, low-cost-, and mass-production. Direct deposition of Cr-PBA on a Cr electrode forms a favorable combination for the spin thermoelectric heterostructure with a seamless interface allowing efficient spin pumping from a thermally driven spin flow. In particular, the observed low Gilbert damping constant shows molecule-based magnetic films could be outstanding platforms for the generation and transmission of magnon in various spin-based electronic applications.

## Reference

1.      Kirihara, A.;   Uchida, K.;   Kajiwara, Y.;   Ishida, M.;   Nakamura, Y.;   Manako, T.;   Saitoh, E.; Yorozu, S., Spin-current-driven thermoelectric coating. *Nat Mater* **2012,** *11* (8), 686-9.
2.      Uchida, K.-i.;   Adachi, H.;   Kikkawa, T.;   Kirihara, A.;   Ishida, M.;   Yorozu, S.;   Maekawa, S.; Saitoh, E. J. P. o. t. I., Thermoelectric generation based on spin Seebeck effects. *Proceedings of the IEEE* **2016,** *104* (10), 1946-1973.
3.      Collet, M.;   de Milly, X.;   d'Allivy Kelly, O.;   Naletov, V. V.;   Bernard, R.;   Bortolotti, P.;   Ben Youssef, J.;   Demidov, V. E.;   Demokritov, S. O.;   Prieto, J. L.;   Munoz, M.;   Cros, V.;   Anane, A.;   de Loubens, G.; Klein, O., Generation of coherent spin-wave modes in yttrium iron garnet microdiscs by spin-orbit torque. *Nat Commun* **2016,** *7,* 10377.
4.      Jungfleisch, M. B.;   Chumak, A. V.;   Kehlberger, A.;   Lauer, V.;   Kim, D. H.;   Onbasli, M. C.; Ross, C. A.;   Klaui, M.; Hillebrands, B., Thickness and power dependence of the spin-pumping effect in Y3Fe5O12/Pt heterostructures measured by the inverse spin Hall effect. *Phys Rev B* **2015,** *91* (13).
5.      Chang, F. J.;   Lin, J. G.; Huang, S. Y., Robust spin current generated by the spin Seebeck effect. *Phy Rev Mater* **2017,** *1* (3).
6.      Guo, E. J.;   Cramer, J.;   Kehlberger, A.;   Ferguson, C. A.;   MacLaren, D. A.;   Jakob, G.; Klaui, M., Influence of Thickness and Interface on the Low-Temperature Enhancement of the Spin Seebeck Effect in YIG Films. *Phys Rev X* **2016,** *6* (3), 031012.
7.      Fang, L.;   Bozdag, K. D.;   Chen, C. Y.;   Truitt, P. A.;   Epstein, A. J.; Johnston-Halperin, E., Electrical spin injection from an organic-based ferrimagnet in a hybrid organic-inorganic heterostructure. *Phys Rev Lett* **2011,** *106* (15), 156602.
8.      Yoo, J.-W.;   Chen, C.-Y.;   Jang, H.;   Bark, C.;   Prigodin, V.;   Eom, C.; Epstein, A. J. N. m., Spin injection/detection using an organic-based magnetic semiconductor. *Nat Mater* **2010,** *9* (8), 638-642.
9.      Liu, H.;   Zhang, C.;   Malissa, H.;   Groesbeck, M.;   Kavand, M.;   McLaughlin, R.;   Jamali, S.; Hao, J.;   Sun, D.; Davidson, R. A. J. N. m., Organic-based magnon spintronics. *Nat Mater* **2018,** *17* (4), 308.
10.     Sato, O.;   Iyoda, T.;   Fujishima, A.; Hashimoto, K. J. S., Electrochemically tunable magnetic phase transition in a high-Tc chromium cyanide thin film. *Science* **1996,** *271* (5245), 49-51.
11.     Mallah, T.;   Thiebaut, S.;   Verdaguer, M.; Veillet, P., High-T(C) Molecular-Based Magnets - Ferrimagnetic Mixed-Valence Chromium(Iii)-Chromium(Ii) Cyanides with T(C) at 240-Kelvin and 190-Kelvin.

*Science* **1993,** *262* (5139), 1554-1557.

12.     Coronado, E.;   Makarewicz, M.;   Prieto-Ruiz, J. P.;   Prima-García, H.; Romero, F. M. J. A. M., Magneto-optical properties of electrodeposited thin films of the molecule-based magnet Cr5. 5 (CN) 12· 11.5 H2O. *Adv. Mater.* **2011,** *23* (37), 4323-4326.

13.     Holmes, S. M.; Girolami, G. S. J. J. o. t. A. C. S., Sol− Gel Synthesis of KVII [CrIII (CN) 6]⊙ 2H2O: A Crystalline Molecule-Based Magnet with a Magnetic Ordering Temperature above 100° C. *J. Am. Chem. Soc.* **1999,** *121* (23), 5593-5594.

14.     Ferlay, S.;   Mallah, T.;   Ouahes, R.;   Veillet, P.; Verdaguer, M., A Room-Temperature Organometallic Magnet Based on Prussian Blue. *Nature* **1995,** *378* (6558), 701-703.

15.     Garde, R.;   Villain, F.; Verdaguer, M., Molecule-based room-temperature magnets: catalytic role of V(III) in the synthesis of vanadium-chromium Prussian blue analogues. *J Am Chem Soc* **2002,** *124* (35), 10531-8.

16.     Cahill, D. G., Thermal-Conductivity Measurement from 30-K to 750-K - the 3-Omega Method. *Rev Sci Instrum* **1990,** *61* (2), 802-808.

17.     Muthusamy, S.;   Charles, J.;   Renganathan, B.; Sastikumar, D., In situ growth of Prussian blue nanocubes on polypyrrole nanoparticles: facile synthesis, characterization and their application as fiber optic gas sensor. *J Mater Sci* **2018,** *53* (22), 15401-15417.

18.     Ruiz, E.;   Rodríguez-Fortea, A.;   Alvarez, S.; Verdaguer, M. J. C. A. E. J., Is it possible to get high TC magnets with Prussian blue analogues? A theoretical prospect. *Chem. Eur. J.* **2005,** *11* (7), 2135-2144.

19.     Pokhodnya, K. I.;   Pejakovic, D.;   Epstein, A. J.; Miller, J. S., Effect of solvent on the magnetic properties of the high-temperature V[TCNE](x) molecule-based magnet. *Phys Rev B* **2001,** *63* (17).

20.     Cahill, D. G.; Pohl, R. O., Thermal-Conductivity of Amorphous Solids above the Plateau. *Phys Rev B* **1987,** *35* (8), 4067-4073.

21.     Cahill, D. G., Thermal conductivity measurement from 30 to 750 K: the 3*w* method. *Rev Sci Instrum* **1990,** *61* (2), 802-808.

22.     Yang, B.;   Liu, J. L.;   Wang, K. L.; Chen, G., Simultaneous measurements of Seebeck coefficient and thermal conductivity across superlattice. *Appl. Phys. Lett.* **2002,** *80* (10), 1758-1760.

23.     Kehlberger, A.;   Ritzmann, U.;   Hinzke, D.;   Guo, E. J.;   Cramer, J.;   Jakob, G.;   Onbasli, M. C.; Kim, D. H.;   Ross, C. A.;   Jungfleisch, M. B.;   Hillebrands, B.;   Nowak, U.; Klaui, M., Length Scale of the Spin Seebeck Effect. *Phys. Rev. Lett.* **2015,** *115* (9).

24.     Guo, E. J.;   Cramer, J.;   Kehlberger, A.;   Ferguson, C. A.;   MacLaren, D. A.;   Jakob, G.; Klaui, M., Influence of Thickness and Interface on the Low-Temperature Enhancement of the Spin Seebeck Effect in YIG Films. *Phys. Rev. X* **2016,** *6* (3).

25.     Nadeem, K.; Krenn, H., Exchange Bias, Memory and Freezing Effects in NiFe2O4 Nanoparticles. *J Supercond Nov Magn* **2011,** *24* (1-2), 717-720.

# Chapter 5. Microwave driven spin pumping in Molecule-based Prussian blue/Cr heterostructure

In this chapter I first introduce molecule-based magnet for magnon generation and spin pumping into metal layer using microwaves. We studied the generation, propagation, and detection of magnon in the Cr-PBA/Cr through ferromagnetic resonance (FMR) and FMR with inverse spin Hall effect (FMR-ISHE) experiments. Both FMR and FMR-ISHE measurements were done with coplanar waveguide.

## 5.1 Ferromagnetic Resonance measurements

If the precession frequency of the magnetization in a ferromagnet with Larmor frequency coincide with microwave frequency, the power of microwave is absorbed into precessing magnetization representing absorption peak. The FMR spectra are observed by the power absorption. The FMR spectra were recorded with sweeping the external magnetic field at microwave frequencies in the range of 3-19 GHz (Fig. 44). The resonance field ($H_R$) and linewidth ($\Delta H$) of FMR spectra were extracted from the first derivative of Lorentzian, as follows

$$\frac{dP}{dH_{DC}} = K_1 \frac{4\Delta H(H-H_R)}{[4(H-H_R)^2+(\Delta H)^2]^2} - K_2 \frac{[(\Delta H)^2-4(H-H_R)^2]}{[4(H-H_R)^2+(\Delta H)^2]} + \text{slope}H + \text{offset}$$

The dependence of the resonance field ($H_R$) on the microwave frequency can be well described with the Kittel equation, $\nu = \frac{\gamma}{2\pi}[H_R(H_R + \mu_0 M_s)]^{1/2}$, where $\nu$ is microwave frequency, $\gamma$ is the gyromagnetic factor, $H_R$ is a resonance field, $M_s$ is a saturation magnetization. Fitting with Kittel equation produces $M_s$ = 12.676 kA/m and g-factor = 1.96 (Fig. 45). The frequency dependence of $\Delta H$ of FMR spectra in Cr-PBA/Cr heterostructures can provide the effective Gilbert damping constant ($\alpha_{\text{eff}}$) following the relation,

$$\Delta H = \Delta H_0 + \frac{4\pi\nu\alpha_{\text{eff}}}{\sqrt{3}\gamma},$$

where, $\Delta H_0$ denotes an inhomogeneous broadening by structural imperfections. The obtained effective Gilbert damping constant for the Cr-PBA (1.4 μm)/Cr (10 nm) heterojunction was $\alpha_{\text{eff}} = 7.5 \times 10^{-4}$ (Fig. 46). We also recorded FMR spectra of Cr-PBA/Cr heterojunctions with varying thickness $d$ of Cr-PBA films. The frequency dependence of FMR spectra provides $\alpha_{\text{eff}}$ for Cr-PBA/Cr heterojunctions of different $d$. Then, intrinsic damping constant ($\alpha_0$) of the Cr-PBA film and spin mixing conductance ($g_{\text{eff}}^{\uparrow\downarrow}$) of the heterojunction can be estimated following the equation [1],

$$\alpha_{\text{eff}} = \alpha_0 + \Delta\alpha = \alpha_0 + \frac{g\mu_B}{4\pi M_s d} g_{\text{eff}}^{\uparrow\downarrow},$$

where $\Delta\alpha$ is the additional Gilbert damping caused by spin pumping. Fig. 46 shows thickness dependence of the measured effective damping constant ($\alpha_{\text{eff}}$). Here, we assume constant value of the spin mixing conductance, $g_{\text{eff}}^{\uparrow\downarrow}$, because the fabrications of Cr-PBA/Cr heterostructures were done under the same condition. Fitting with the equation 6 produces estimated values of $\alpha_0 = (2.4\pm0.67)\times10^{-4}$ and $g_{\text{eff}}^{\uparrow\downarrow} = (6.5\pm0.52)\times10^{18}$ m$^{-2}$, which are comparable to those of the YIG and YIG/Pt [1, 2].



**Figure 44** First derivative FMR spectra of the Cr-PBA (1.4 μm)/Cr (10 nm) heterojunction at various microwave frequencies measured at 100 K. The recorded data are fitted by using the derivative of Lorentzian function.



**Figure 45.** Frequency dependence of resonance field $H_R$.

**Figure 46.** FWHM as increasing the frequency of rf field. The slope of a linear fit produces low effective Gilbert damping constant, $\alpha_{\text{eff}} \sim 7.5\times10^{-4}$.



**Figure 47. Thickness dependent damping constants of Cr-PBA/Cr heterojunctions.** For the calculation of the intrinsic damping constant of the Cr-PBA film, we measured FMR for Cr-PBA thickness ranging from 650 nm to 1.4 μm.

## 5.2 Micro-driven Inverse spin Hall effect measurements



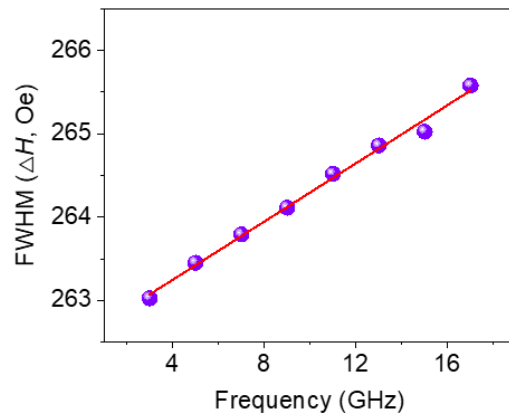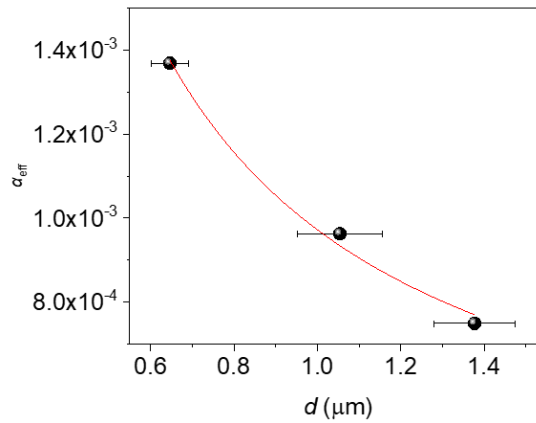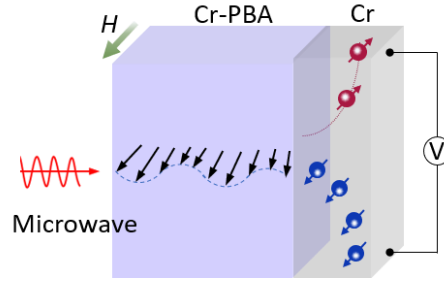The conversion of spin angular momentum into an electric current in the Cr-PBA/Cr heterojunction was studied further through FMR-driven ISHE as illustrated in the upper illustration. Fig. 48 displays measured $V_{ISHE}$ at continuous microwave $f = 9$ GHz in Cr-PBA/Cr heterojunction. Both $\Delta H$ and $H_R$ of $V_{ISHE}$ are in consistent with those of FMR spectra shown in Fig. 44. This clearly suggests that the measured $V_{ISHE}$ originates from FMR-generated magnon flow in the Cr-PBA film. The transferred spin current density $j_s^0$ at the interface can be determined from the relation,

$$J_s^0 = \frac{g_{eff}^{\uparrow\downarrow} \gamma^2 H_1^2 \hbar \left[ 4\pi M_s \gamma \sin \theta_M^2 + \sqrt{(4\pi M_s)^2 \gamma^2 + 4\omega^2} \right]}{8\pi \alpha_{eff}^2 \left[ (4\pi M_s)^2 \gamma^2 \sin \theta_M^4 + 4\omega^2 \right]},$$

where $H_1$ is rf field and $\theta_M$ is the angle between the magnetization direction and the film normal. Then, the spin Hall angle ($\theta_{SHE}^{Cr}$), a figure of merit for the conversion between the transferred spin current and charge current, can be estimated following the relation,

$$V_{ISHE} = \frac{2e}{\hbar} \frac{\theta_{SHE}^{Cr} \lambda_s^{Cr} \omega J_s^0}{\sigma^{Cr} d^{Cr}} \tanh \left( \frac{2d^{Cr}}{\lambda_s^{Cr}} \right),$$

where $\lambda_s^{Cr}$ and $\sigma^{Cr}$ are the spin diffusion length and conductivity of the Cr layer, respectively. We took $\lambda_s^{Cr} = 2.1$ nm from literature [3] and the value of $\sigma^{Cr}$ from the 4-terminal measurement. The obtained spin Hall angle ($\theta_{SHE}^{Cr}$) $\sim -0.0051$. This value is within the range of $\theta_{SHE}^{Cr}$ values in the literature [3, 4]. In short, the studies of FMR and FMR-ISHE demonstrate the effective generation of spin flow in Cr-PBA and spin-pumping process into the adjacent Cr layer.
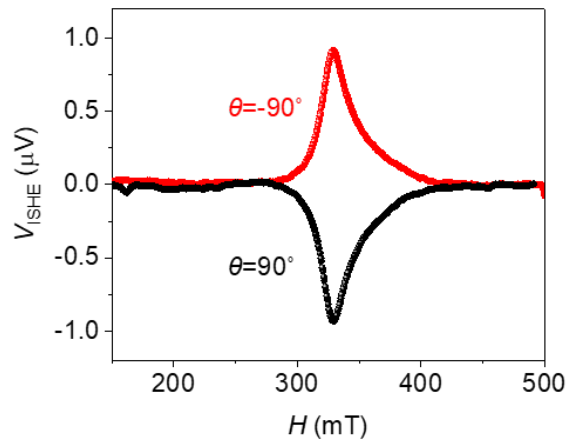
**Figure 48.** $V_{ISHE}$ ($H$) measured for Cr-PBA (1.4 μm)/Cr (10 nm) bilayer upon applying 9 GHz of microwave. The peak of $V_{ISHE}$ corresponds to the resonance field $H_R$ of FMR.
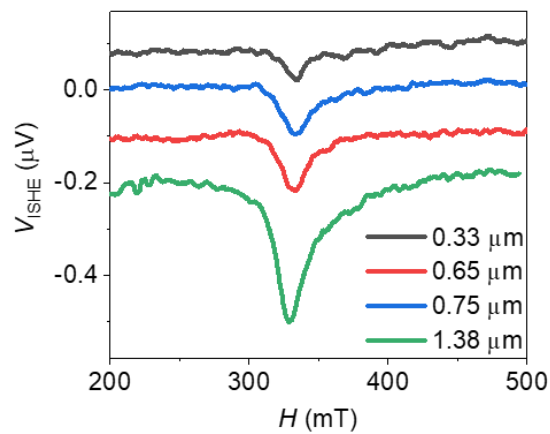


**Figure 49.** $V_{ISHE}$ ($H$) of Cr-PBA/Cr heterojunctions with various Cr-PBA thicknesses.

## Reference

1.      Jungfleisch, M. B.;   Chumak, A. V.;   Kehlberger, A.;   Lauer, V.;   Kim, D. H.;   Onbasli, M. C.;   Ross, C. A.;   Klaui, M.; Hillebrands, B., Thickness and power dependence of the spin-pumping effect in $Y_3Fe_5O_{12}$/Pt heterostructures measured by the inverse spin Hall effect. *Phys. Rev. B* **2015,** *91* (13), 134407.

2.      Collet, M.;   de Milly, X.;   d'Allivy Kelly, O.;   Naletov, V. V.;   Bernard, R.;   Bortolotti, P.;   Ben Youssef, J.;   Demidov, V. E.;   Demokritov, S. O.;   Prieto, J. L.;   Munoz, M.;   Cros, V.;   Anane, A.;   de Loubens, G.; Klein, O., Generation of coherent spin-wave modes in yttrium iron garnet microdiscs by spin-orbit torque. *Nat. Commun.* **2016,** *7*, 10377.

3.      Qu, D.;   Huang, S. Y.; Chien, C. L., Inverse spin Hall effect in Cr: Independence of antiferromagnetic ordering. *Phys. Rev. B* **2015,** *92* (2), 020418.

4.      Du, C. H.;   Wang, H. L.;   Yang, F. Y.; Hammel, P. C., Systematic variation of spin-orbit coupling with *d*-orbital filling: Large inverse spin Hall effect in 3*d* transition metals. *Phys. Rev. B* **2014,** *90* (14), 140407(R).

# Chapter 6. Conclusion and directions for further research

## 6.1 Summary and conclusions

For the STE energy harvesting, we developed the solution-processed high quality YIG thin film showing the great performance of thermal energy conversion with combination of Pt. And we introduced the new class of magnetic materials, PBA which has potentiality for the substantial magnon excitation more than that of inorganic magnets. Especially, the studied molecule-based magnetic films carry a number of advantageous characteristics over inorganic magnetic insulators along with flexible film fabrication processing. Conventional electrochemical deposition at room temperature was successfully employed for the fabrication of the Cr-PBA based STE device. This deposition technique can be easily adopted for the large-area-, and mass-production of thin film and boost an important merit of STE, *i.e.* large-area scalability. Various methodologies, such as painting and printing, will be also utilized for developing the PBA film. Excitations of low energy magnons in this class of magnet are much stronger than those in the typical inorganic magnets. Moreover, the obtained the low Gilbert damping constant, comparable to that of the epitaxial YIG film, grants the transport of thermally excited magnons over the long distance with low loss. Furthermore, the low thermal conductivity in the studied molecule-based magnetic film is a benefit for STE energy harvesting because it assists maintaining a higher temperature gradient across the film.

In short, the development of molecule-based magnet PBA can be contributory to the development of ferrimagnetic materials for the effective magnon excitation and its application of STE. These alternative route of ferrimagnetic synthesis will enhance the STE energy harvesting as well as promising platforms for the generation and transmission of magnons in various spin-based electronic applications.

## 6.2 Toward the Future

**Consecutive research of STE energy conversion by developing high $T_c$ molecule-based magnet**

For the usage of thermoelectric energy conversion in our life, the devices should operate at room temperature properly. As I wrote in the chapter 4-5, the molecule-based magnet shows the effective magnon excitation, the low damping constant, and the low thermal conductivity for an application of the spin thermoelectric generation layer with the facile process at room temperature and in the ambient atmosphere. Furthermore, by using the ECD we can directly deposit the film on various metallic electrodes. Thus, I will develop the high $T_c$ molecule-based magnet and investigate the magnon excitation, spin injection from the magnet into metals, and damping behaviors in room temperature. For the development, various chemical materials for ECD will be employed by the followed steps. First, it is important to find the substitution of $Cr^{2+}$ ions. The substitution ions should be liable, reactive with $[Cr^{III}(CN)_6]^{3-}$, and have the exchange interaction with $Cr^{III}$ spins effectively, such as V ion. Second, the proper electric potential ($E$) should be founded with the reference electrode. After the synthesis of films, we can observe the crystallization, roughness, and magnetization of the films. So, I will find the optimized condition for the film fabrication. Third, the damping behavior, spin injection from the magnet into the metal electrode should be investigated by FMR and ISHE-FMR. Finally, the effective spin thermoelectric energy convertor will be introduced for the room temperature molecule-based STE.

**Molecule-based magnet/TMDC heterojunction for spinterface and STE application.**

To enhance the spin injection rate at the interface between molecule-based magnet and metal layer, the sharp interface is needed with large spin mixing conductance. For this, I am trying to introduce transition metal dichalcogenides (TMDCs) as a working electrode of ECD. Since TMDCs are composed with large atomic numbers and has spin-momentum locking state ($PtSe_2$, $PtTe_2$, $WTe_2$), it invokes large spin Hall angle and spin Hall conductivity at the heterojunction with magnetic materials. TMDCs have various unique properties, for example, great large magnetoresistance [1], modulation of electronic and optical properties by doping [2], and controllability in spin-orbit coupling of adjacent layer [3]. I'm especially interested in its large spin orbit coupling properties [4, 5]. Hence, I will try to adapt them into working electrode of ECD for the deposition of molecule-based magnets. The TMDCs does not shows any hydrogenation reactions at the electric potential of the reduction for $Cr^{3+}$ unlike the noble metals (Pt, Pd). I will fabricate a sharp spinterface for the effective spin-charge conversion in the heterojunction of molecule-based magnet/TMDC and then investigate the spin generation and the spin-charge conversion in the heterojunction for the STE application.

## Reference

1.      Ali, M. N.;   Xiong, J.;   Flynn, S.;   Tao, J.;   Gibson, Q. D.;   Schoop, L. M.;   Liang, T.;   Haldolaarachchige, N.;   Hirschberger, M.;   Ong, N. P.; Cava, R. J., Large, non-saturating magnetoresistance in WTe2. *Nature* **2014,** *514* (7521), 205-+.

2.      Debbichi, M.;   Debbichi, L.; Lebegue, S., Controlling the stability and the electronic structure of transition metal dichalcogenide single layer under chemical doping. *Phys Lett A* **2019,** *383* (24), 2922-2927.

3.      Safeer, C. K.;   Ingla-Aynes, J.;   Herling, F.;   Garcia, J. H.;   Vila, M.;   Ontoso, N.;   Calvo, M. R.;   Roche, S.;   Hueso, L. E.; Casanova, F., Room-Temperature Spin Hall Effect in Graphene/MoS2 van der Waals Heterostructures. *Nano Lett* **2019,** *19* (2), 1074-1082.

4.      Ghiasi, T. S.;   Kaverzin, A. A.;   Blah, P. J.; van Wees, B. J., Charge-to-Spin Conversion by the Rashba-Edelstein Effect in Two-Dimensional van der Waals Heterostructures up to Room Temperature. *Nano Lett* **2019,** *19* (9), 5959-5966.

5.      Manchon, A.;   Koo, H. C.;   Nitta, J.;   Frolov, S. M.; Duine, R. A., New perspectives for Rashba spin-orbit coupling. *Nat Mater* **2015,** *14* (9), 871-882.

# Acknowledgements

I would like to express the deepest appreciation to my advisor, Prof. Jung-Woo Yoo, for the patient guidance encouragement, and advices which he has provided throughout my times as his student. He had brought me to the world of "spintronics" and had been very supportive of spin thermoelectricity and cheer me up all the time with teaching me of meaning of my research. Whenever I fall down frustration, he woke me up with encouraging me to keep working well. Without his guidance and persistent helps I wouldn't have found a way to pave the way for my research.

I would like to thank my committee members, Prof. Hyung-Joon Shin, Prof. Jae sung Son, Prof. Joonki Suh, and Prof. Jong-Ryul Jeong. Thanks to their valuable comments and advices, I notice what I overlooked and the new insights from various viewpoints.

There are a lot of people I would like to express my gratitude to for their helps, supports and friendships during my Ph.D. study. I must express my gratitude to Dr. Jungmin Park for his sincere helps and discussions for a long time and he helped me to complete my work with RND ware co. And I would like to thank to my forever senior, Dr. Junhyeon Jo. He thought me how to plan and process my researches and experiments successfully in detail. I would like to express my gratitude to him again. I also thank my senior, Dr. Mijin Jin, for her advises to encourage me and lead to good way of me. And also, I would like to thank my precious companies, Deaseong choe, Hyeonjung jeong, Jonghyeon Choi, Jeabyeong Lee, Seonghyeon Lee, and Seunghyun Noh. I used to talk with them about my personal worries as well as research projects. Thanks to my lab members, I could have spent wonderful and meaningful time and arrived the terminal of my degree without any serious problems during Ph.D.

I would like to express my love to my graduate friends, Min-Ji Kim, Na-Hyang Kim, Jeong-Hyun Woo, and Chang Hee Hong . I have relied on my friends a lot and we have shared lots of memories for over five years, and our friendship will last even after graduation. And I had a few more good friends in graduate school, so I was able to get through the hard times well. I also would like to thank my college friends for sending me messages of support all the time, especially Jung Hwan Yoon, Hyunsung Kim, Jeongah Seo, Yun Hee Park and Eun Bi Kim. And I send a message of deep gratitude to my best friend, Sunshine Yang, who always cheers me up.

Finally, I wish to thank my family for their love and support throughout my entire life. I dedicate this thesis to my most respected parents, Chang-Ho Oh and Hyeon-Jin Kim.

# CURRICULUM VITAE

**INSEON OH**

The School of Materials Science and Engineering

Ulsan National Institute of Science and Technology (UNIST)

Email: sunnyooh@unist.ac.kr

Phone: +82-10-6423-0577

## EDUCATION

◆ **M.S. & Ph.D.** Ulsan National Institute of Science and Technology    (Mar. 2015 - )

   **Major** : The School of Materials Science and Engineering

   **Research Advisor** : Prof. Jung-Woo Yoo

   **Thesis Title** : Spin thermoelectric energy conversion based-on hybrid magnetic insulator

◆ **B.S.** Chonnam National University                                     (Mar. 2011 – Fab. 2015)

   **Major** : School of chemical engineering

## RESEARCH THEME

◆ **Major research**

   - Spin Caloritronics

   - Spin-charge conversion

   - Magnetic Physics in organic materials

◆ **Minor research**

   - Thermoelectricity

   - Field effect transistor (FET) in graphene and 2DEG

## EXPERIMENTAL SKILLS

◆ **Device fabrication**

- Thin film deposition:

  Thermal-, Electron beam-, Atomic layer-, Spin coating-, Electrochemical deposition

- Device patterning:

  Photolithography, Electron beam lithography, Wet & Dry etching


◆ **Measurement**

- Electrical transport:

  DC & AC (Keithley 2400, 2636A, 2182A, 6221, 617) instruments, PPMS. LabView

- Magnetometry:

  SQUID-VSM (MPMS3)

- Thermoelectric transport:

  Thermal Transport option in PPMS, Home-made equipment, $3\omega$ method for thermal conductivity measurement.

- Microwave transport:

  FMR, ISHE-FMR

- Analysis

  SEM, AFM, Raman, UV-vis, XRD

## PUBLICATIONS

1. **I. Oh**[¶], J. Park, D. Choe, J. Jo, H. Jeong, M.-J. Jin, Y. Jo, J. Suh, B.-C, Min, J.-W. Yoo*, "Molecule-based magnetic thin film for spin-thermoelectric energy conversion." – Submitted for publication

2. Y. Jiang[¶], **I. Oh**[¶], S. H. Joo[¶], Y.-S. Seo, S. H. Lee, W.K. Seong, Y. J. Kim, J. Hwang, S.K. Kwak*, J.-W. Yoo*, and R. S. Ruoff*, "Synthesis of a Copper 1,3,5-Triamino-2,4,6-Benzenetriol Metal-Organic Framework that is Metallic when Doped with Iodine" – under revision in " *Journal of the American Chemical Society*

3. J. Park[¶], **I. Oh**, M.-J. Jin, J. Jo, D. Choe, H. D. Yun, S. W. Lee, Z. Lee, S.-Y. Kwon, H. J., S.B. Chung, J.-W. Yoo*, "Observation of spin-polarized Anderson state around charge neutral point in graphene with Fe-clusters." *Scientific reports*, **10** (1), 1-8 (2020)

4. J. Jo[¶], J. Byun, J. Lee, D. Choe, **I. Oh**, J. Park, M.-J. Jin, J. Lee, J.-W Yoo* "Emergence of Multispinterface and Antiferromagnetic Molecular Exchange Bias via Molecular Stacking on a Ferromagnetic Film." *Advanced Functional Materials*, **30** (11), 1908499 (2020)

5. J. Park[¶], **I. Oh**, A.Y. Lee, H. Jang, J.-W. Yoo, Y. Jo, S.Y. Park*, "The effect of graphene interlayer at Pt/YIG interface on spin pumping." *Journal of Alloys and Compounds*, **829**, 154534 (2020)

6. J. Hong[¶], E. D. Jung, J. C. Yu, D. W. Kim, Y. S. Nam, **I. Oh**, E. Lee, J.-W. Yoo, S. Cho, M. H. Song*, "Improved Efficiency of Perovskite Solar Cells Using a Nitrogen Doped Graphene Oxide Treated Tin Oxide Layer", *ACS applied materials & interfaces*, **12**, 2417-2423 (2020)

7. Y. Jiang[¶], **I. Oh**[¶], S. H. Joo[¶], O. Buyukcakir, X. Chen, S. H. Lee, M. H., W. K. Seong, S. K. Kwak*, J.-W. Yoo*, R. S Ruoff*, "Partial Oxidation-Induced Electrical Conductivity and Paramagnetism in a Ni (II) Tetraaza [14] annulene-Linked Metal Organic Framework." *Journal of the American Chemical Society*, **141** (42), 16884-16893 (2019)

8. D. Choe[¶], M.-J. Jin[¶], S.-I. Kim, H.-J. Choi, J. Jo, **I. Oh**, J. Park, H. Jin, H. C. Koo, B.-C. Min, S. Hong, H.-W. Lee, S.-H. Baek, J.-W. Yoo*, "Gate-tunable giant nonreciprocal charge transport in noncentrosymmetric oxide interfaces." *Nature communications*, **10** (1), 1-8 (2019)

9. Y. Jiang[¶], **I. Oh**[¶], S. H. Joo[¶], S. K. Kwak*, J.-W. Yoo*, R. S. Ruoff*, "Organic Radical-Linked Covalent Triazine Framework with Paramagnetic Behavior." *ACS Nano*, **13** (5), 5251-5258 (2019)

10. M.-J. Jin[¶], S.-I. Kim, S.Y. Moon, D. Choe, J. Park, V. Modepalli, J. Jo, **I. Oh**, S.-H. Baek, J.-W. Yoo*, "Study of Rashba Spin–Orbit Field at LaAlO$_3$/SrTiO$_3$ Heterointerfaces." *Journal of Electronic Materials*, **48** (3), 1347-1352 (2019)

11. M.-J. Jin[¶], D. Choe, S.Y. Lee, J. Park, J. Jo, **I. Oh**, S.-I. Kim, S.-H. Baek, C. Jeon, J.-W. Yoo*,

"Probing surface electronic properties of a patterned conductive STO by reactive ion etching.", *Applied Surface Science*, **466**, 730-736 (2019)

12. J. Jo¶, J. Byun, **I. Oh**, J. Park, M.-J. Jin, B.C. Min, J. Lee, J.-W. Yoo*, "Molecular Tunability of Magnetic Exchange Bias and Asymmetrical Magnetotransport in Metalloporphyrin/Co Hybrid Bilayers." *ACS nano*, 13 (1), 894-903 (2018)

13. **I. Oh**¶, J. Park¶, J. Jo, M.-J. Jin, M.S. Jang, K.S. Lee, J.W. Yoo*, "Solution-Processed Ferrimagnetic Insulator Thin Film for the Microelectronic Spin Seebeck Energy Conversion.", *ACS applied materials & interfaces*, **10** (34), 28608-28614 (2018)

14. M.H. Jeong¶, A. Sanger, S.B. Kang, Y.S. Jung, **I. Oh**, J.-W Yoo, G.H. Kim, K.J. Choi* "Increasing the thermoelectric power factor of solvent-treated PEDOT: PSS thin films on PDMS by stretching", *Journal of Materials Chemistry A*, **6** (32), 15621-15629 (2018)

15. J. Jo¶, **I. Oh**, M.-J Jin, J. Park, J.S. Son, K.S. An, J.-W. Yoo*, "Highly stretchable organic thermoelectrics with an enhanced power factor due to extended localization length.", *Organic Electronics*, **50**, 367-375 (2017)

16. J. Park¶, H.D. Yun, M.-J. Jin, J. Jo, **I. Oh**, V. Modepalli, S.Y. Kwon, J.-W Yoo*, "Gate-dependent spin Hall induced nonlocal resistance and the symmetry of spin-orbit scattering in Au-clustered graphene", *Physical Review B*, **95**(24), 245414 (2017)

17. **I. Oh**¶, J. Jo, J. Park, J. Lee, H. Shin, J.-W. Yoo*, "Local crystallization and enhanced thermoelectric performance of glassy carbon induced by the electron beam irradiation.", *Current Applied Physics*, **16,** 1511-1516 (2016).